



Calibration strategies of PDC kinetic energy models and their application to the construction of hazard maps

A. Aravena, A. Bevilacqua, M. De' Michieli Vitturi, T. Esposti Ongaro, A. Neri, R. Cioni

► To cite this version:

A. Aravena, A. Bevilacqua, M. De' Michieli Vitturi, T. Esposti Ongaro, A. Neri, et al.. Calibration strategies of PDC kinetic energy models and their application to the construction of hazard maps. Bulletin of Volcanology, 2022, 84 (3), pp.29. 10.1007/s00445-022-01538-8 . hal-03577294

HAL Id: hal-03577294

<https://uca.hal.science/hal-03577294>

Submitted on 16 Feb 2022

HAL is a multi-disciplinary open access archive for the deposit and dissemination of scientific research documents, whether they are published or not. The documents may come from teaching and research institutions in France or abroad, or from public or private research centers.

L'archive ouverte pluridisciplinaire **HAL**, est destinée au dépôt et à la diffusion de documents scientifiques de niveau recherche, publiés ou non, émanant des établissements d'enseignement et de recherche français ou étrangers, des laboratoires publics ou privés.

[Click here to view linked References](#)

Calibration strategies of PDC kinetic energy models and their application to the construction of hazard maps

A. Aravena^{1,2}, A. Bevilacqua³, M. de' Michieli Vitturi³, T. Esposti Ongaro³, A. Neri³, and R. Cioni¹

¹Dipartimento di Scienze della Terra, Università di Firenze, Firenze, Italy.

²Laboratoire Magmas et Volcans, Université Clermont Auvergne, CNRS, IRD, OPGC, Clermont-Ferrand, France.

³Istituto Nazionale di Geofisica e Vulcanologia, Sezione di Pisa, Pisa, Italy.

Corresponding author: A. Aravena (alvaro.aravena@uca.fr)¹

Keywords: Pyroclastic density currents, volcanic hazard assessment, numerical modeling, kinetic energy models, energy cone model, box model, branching formulation.

Highlights

- We present a set of structured and reproducible strategies to calibrate PDC numerical models.
- We implement these calibration strategies on two user-friendly kinetic energy models: ECGMapProb 2.0 and BoxMapProb 2.0.
- These calibration strategies reduce the biases derived from user choices in the construction of hazard maps.

¹ Authorship statement

All co-authors contributed to the manuscript preparation and the identification of the study cases presented in this paper. AA programmed the models ECGMapProb 2.0 and BoxMapProb 2.0, run simulations and post-processed results. AA, AB, MdMV and TEO worked in the mathematical description of the models and the calibration strategies.

Abstract

The availability of computer tools able to describe the behavior of pyroclastic density currents (PDCs) with uncertainty quantification is of primary importance for the assessment of volcanic hazard. A common strategy to assess the intrinsic variability of these phenomena is based on the analysis of large sets of numerical simulations with variable input parameters. The use of models fast enough to allow for a large number of simulations, such as the so-called kinetic energy models, is thus advantageous. Due to the sensitivity of kinetic energy models to poorly constrained input parameters, the definition of their variation ranges is a critical step in the construction of hazard maps and a numerical calibration becomes necessary. We present a set of reproducible and structured calibration procedures of numerical models based either on a reference deposit or on the distribution of runout distance or inundation area of documented PDCs. In the first case, various metrics can be adopted to compare the model results with the reference PDC deposit (root mean square distance, Hausdorff distance and Jaccard index), facilitating the development of scenario-based hazard assessments. Calibrations based on the distribution of runout distance or inundation area allow the construction of probabilistic hazard maps that are not conditioned on the occurrence of a specific scenario, but rather reflect the variability of the documented PDCs during the time window considered. Importantly, our calibration strategies allow one to set the input parameters considering their potential statistical dependence. These procedures have been implemented on the user-friendly versions of two kinetic energy models: EMapProb 2.0 and BoxMapProb 2.0, whose functionalities are presented for the first time in this paper. The different calibration strategies and the functionalities of the two programs are illustrated by considering three case studies: El Misti (Peru), Merapi (Indonesia) and Campi Flegrei (Italy).

1. Introduction

42 Pyroclastic density currents (PDCs) are mixtures of gas, juvenile pyroclasts and lithic fragments
43 typically produced by a lateral blast or by the collapse of an eruptive column or a volcanic dome
44 (Druitt 1998; Roche et al. 2013; Dufek et al. 2015; Lube et al. 2020). These mixtures are denser
45 than the surrounding atmosphere and propagate laterally due to the effects of gravity and inertia,
46 and are influenced by the volcano topography. PDCs represent one of the major hazards associated
47 with volcanic systems, which have been systematically assessed by adopting an approach based
48 on numerical modeling (Malin and Sheridan 1982; Neri et al. 2015a, 2022; Sheridan et al. 2004;
49 Patra et al. 2005; Kelfoun et al. 2009; Doyle et al. 2010; Esposti Ongaro et al. 2011; 2016; Kelfoun
50 2011; de' Michieli Vitturi et al. 2019; Aravena et al. 2020). PDCs pose important modeling
51 challenges because of their complex propagation dynamics and the uncertainty in their initial
52 conditions. Due to this uncertainty, a common strategy to assess the intrinsic variability of these
53 phenomena is based on the analysis of a large number of simulations (e.g. 10^4 - 10^6) derived from
54 the sampling of a statistically representative set of input parameters (Neri et al. 2015b; Tierz et al.
55 2016a; Bevilacqua et al. 2017; Rutarindwa et al. 2019; Patra et al. 2020). Consequently, tools fast
56 enough to allow for large numbers of simulations are required, such as the so-called kinetic energy
57 models (Roche et al. 2013; Aravena et al. 2020). These models are based on the calculation of the
58 kinetic energy in the flow front as a function of the distance travelled by the PDC. Kinetic energy
59 is compared with the potential energy associated with the topographic obstacles encountered by
60 the PDC to calculate the runout distance. Other strategies to reduce computational cost in
61 uncertainty quantification studies include Gaussian emulators (Bayarri et al. 2009; 2015; Anderson
62 et al. 2019; Poland and Anderson 2019) and Polynomial Chaos expansions (Dalbey et al., 2008;
63 Tierz et al., 2018). These approaches enable the quick production of hazard maps without an
64 excessive computational expense (e.g., they can be run on a single computer processor in less than

an hour) and have important applications in computationally-light e-tools for rapid volcanic hazard and risk-management (Tonini et al. 2015; Marti et al. 2016; Bartolini et al. 2017; Takarada et al. 2017; Gallant et al. 2018). In the case of kinetic energy models, because of their sensitivity on often poorly-constrained input parameters, the definition of variation ranges for model inputs is a critical step in the construction of statistically reliable hazard maps.

The absence of standardized strategies to set the input parameters of kinetic energy models often limits the capability to perform comparative analyses between field data and numerical models. Inter-comparison of models is a critical step in the validation of numerical tools, as discussed by Esposti Ongaro et al. (2020a), being particularly relevant when these tools are used to define measures of volcanic risk mitigation (Valentine 2019; Gueugneau et al. 2021). We stress that there are similar difficulties in any numerical model when it is adopted to describe a physical phenomenon characterized by significant uncertainty (Scollo et al. 2008; Worni et al. 2012; Biass et al. 2016; White et al. 2017; Charbonnier et al. 2018; de' Michieli Vitturi and Tarquini 2018; Aspinall and Woo 2019; Bevilacqua et al. 2019; Yang et al. 2020), supporting the importance of developing strategies to address this issue.

In this context, we present a set of reproducible and structured procedures to calibrate the input parameters of PDC numerical models based on geological information of the volcanic system of interest. These calibration strategies reduce the biases derived from user assumptions in the construction of PDC hazard maps, which are often necessary due to data incompleteness. The geological information used in these calibration strategies can be described in terms of the inundation zone of a specific PDC or the distribution of runout distances or inundation areas of past PDCs. Importantly, these calibration procedures are implemented in the user-friendly programs EMapProb 2.0 and BoxMapProb 2.0, which are based on the traditional and branching

formulations of the energy cone and the box model, respectively (Aravena et al. 2020), and whose functionalities and user manuals are included in this paper (see Supplementary Material).

This study complements many previous efforts to set the input parameters of kinetic energy models based on the eruptive record of volcanoes (e.g. Neri et al. 2015b; Tierz et al. 2016a; 2016b; Ogburn and Calder 2017; Cioni et al. 2020). The purpose of our work is not to compare the suitability of different calibration procedures or provide new hazard maps for well-documented volcanoes, but to present a set of standardized calibration strategies that can be used for the quick construction of PDC inundation probabilistic maps. The applicability of these calibration strategies is not restricted to kinetic energy models, and they can be easily implemented for any numerical model able to simulate the inundation area of PDCs. We illustrate these calibration strategies by considering three volcanic systems: El Misti (Peru), Merapi (Indonesia) and Campi Flegrei (Italy). This paper consists of five sections. In Section 2 we describe briefly the numerical models used in this work and their input parameters. In Section 3 we present a set of reproducible calibration strategies of the inputs of PDC numerical models. In Section 4 we show three illustrative applications of our calibration strategies and, finally, in Section 5 we present a summary and conclusion of this paper.

2. Input parameters of kinetic energy models

Here we briefly describe the input parameters of the traditional and branching formulations of the energy cone (Section 2.1) and the box model (Section 2.2) as well as the historical background on the criteria used to define their input parameters (Section 2.3).

2.1 Energy cone model

The energy cone model is a simple and widely used formulation to study PDC dispersal (Malin and Sheridan 1982; Sheridan and Malin 1983; Wadge and Isaacs 1988) due to its easy

implementation and fast generation of results. This model describes the evolution of the kinetic energy of a frictional flow by considering a constant rate of energy dissipation, which is compared with the potential energy needed to overcome the topographic obstacles along the PDC path. Consequently, this model describes better the dispersal of dense, frictional granular flows (Campbell 2006; Pudasaini and Domnik 2009), although it has been adopted to simulate dilute PDCs as well. In addition to the collapse location ($Q_{0,0}$), the input parameters of this model are: (a) collapse height ($H_{0,0}$, hereafter defined with respect to the topographic elevation at the point $Q_{0,0}$), and (b) energy cone slope ($\tan(\varphi)$). Note that $\tan(\varphi)$ has been frequently named H/L in the literature, where H represents the height difference between the collapse point and the point of maximum runout and L is the distance travelled by the PDC. The parameters $H_{0,0}$ and $\tan(\varphi)$ define a vertical-axis cone whose interaction with the topography gives rise to an inundation area, as shown in Figure 1a-b. Because this model does not consider processes of pyroclast channelization, an enhanced formulation was presented by Aravena et al. (2020), where a *root* energy cone is complemented with *branch* energy cones along the preferential channelization directions of pyroclastic material, whose collapse heights are proportional to the residual potential energy computed in the vicinity of each channelization zone. *Root* and *branch* energy cones are organized in a tree-like array that gives rise to a branching structure (Harris 1963; Asmussen and Hering 1983; Haccou et al. 2005), which is stopped when the *branch* energy cones are not able to increase the inundation area of the modeled PDC (Fig. 1). The branching formulation does not include additional input parameters and thus the calibration procedures described below are valid both for the traditional and the branching formulations.

2.2 Box model

The box model integral formulation, based on the pioneering work of Huppert and Simpson (1980), describes inertial flows such as dilute PDCs (particle volume concentration of the order of 10^{-2} or less). In this model, friction is assumed to be negligible and the flow propagation dynamics is controlled by the hydrostatic pressure contrast and by the momentum dissipation due to particle sedimentation. The input parameters of the box model are (Esposti Ongaro et al. 2016): collapsing volume (V_0), initial concentration of solid particles (ϕ_0), Froude number (Fr), sedimentation velocity (w_s); solid particle density (ρ_p), and ambient gas density (ρ_a). These parameters define a vertical-axis conoid centered at the source position whose intersection with the topography defines the boundary of the inundation area. In this case as well, a new formulation based on the construction of additional (or *branch*) conoids in the zones of preferential channelization was presented by Aravena et al. (2020), which improves the ability of the box model to reproduce channelization processes of pyroclastic material. In the branching formulation, a *root* conoid is complemented with a set of *branch* conoids disposed along the zones of preferential channelization. These conoids are organized in a branching structure (Harris 1963; Asmussen and Hering 1983; Haccou et al. 2005) that is stopped when the *branch* conoids do not increase the inundation area of the modeled PDC (Aravena et al. 2020). The branching formulation does not involve the inclusion of additional input parameters and thus the calibration strategies described in this work are valid both for the traditional and the branching formulations of the box model.

2.3 Setting the input parameters of kinetic energy models: historical background

In the case of the energy cone model, where input parameters are collapse position ($Q_{0,0}$), collapse height ($H_{0,0}$) and the energy cone slope ($\tan(\varphi)$), several efforts have been devoted to constrain $\tan(\varphi)$ (Hsu 1975). Sheridan and Macías (1995) studied the deposits of pyroclastic flows at Colima volcano (Mexico) showing that $\tan(\varphi)$ is influenced by the pyroclastic flow volume.

Hayashi and Self (1992) also found a negative correlation between $\tan(\varphi)$ and flow volume. The statistical correlation between flow volume and $\tan(\varphi)$ was further investigated and quantified in Spiller et al. (2014) and Ogburn et al. (2016). These papers have only partially constrained the expected variability of $\tan(\varphi)$, and thus additional assumptions are needed to set this input parameter. Regarding the parameter $H_{0,0}$, 3D multiphase flow models (e.g. Esposti Ongaro et al. 2020b) have shown that column collapse height is virtually irrelevant in the determination of the flow runout (which is more likely controlled by the mass flow rate feeding the PDC). Consequently, the interpretation of $H_{0,0}$ as a measure of the collapse height may be misleading in PDCs derived from collapsing columns, and thus it should be considered as a model parameter for which a numerical calibration becomes necessary.

In practice, many strategies for setting input parameters for the energy cone approach have been applied during the last decades, including the use of vent opening maps (i.e. spatial density models of the probable locations of new vents). For instance, Alberico et al. (2002) adopted the energy cone model to study PDC propagation at Campi Flegrei (Italy) using a vent opening probability map to define a set of likely collapse positions. In these simulations, input parameters were imposed to consider two scenarios that roughly reflect the typical runout distance of small- and large-scale PDCs in this volcanic system. Other examples where $H_{0,0}$ and $\tan(\varphi)$ were imposed deterministically are Macías et al. (2008) and Ferrés et al. (2013). Tierz et al. (2016b) applied a Monte Carlo strategy to analyze the inundation area and runout distance of past PDCs at Vesuvius and Campi Flegrei, using independent probability distributions for the model inputs. Other examples where a Monte Carlo approach was applied are Sandri et al. (2018) and Clarke et al. (2020).

Regarding the definition of the box model input parameters, Neri et al. (2015b) studied the geological record of Campi Flegrei to define probability distributions of the inundation area of past PDCs, finalizing these data to compute the input conditions (in particular, the flow volume) of a set of simulations through an iterative method of numerical inversion (Bevilacqua 2016). In addition, Neri et al. (2015b) used the vent opening probability maps from Bevilacqua et al. (2015) for the construction of fully probabilistic maps of PDC inundation at Campi Flegrei. Their findings were further extended by Bevilacqua et al. (2017), who detailed the joint effects of vent position and PDC scale. Both Neri et al. (2015b) and Bevilacqua et al. (2017) considered the inundation area as a random variable whose definition is based on the vent location and the geological record of Campi Flegrei, which was therefore used as an input in the box model simulations performed. Tadini et al. (2021) used average deposit thicknesses as a function of distance from the collapse location (Cioni et al. 2020) to constrain the input parameters of the box model for two significantly different PDC units of the AD 79 Vesuvius eruption.

3. Calibration strategies

Calibrating the input parameters of PDC numerical models is a critical step when they are used in the construction of inundation probability maps, even if the Monte Carlo approach is adopted to sample the model inputs. This is because inundation probability maps are not only controlled by the variation range of the input parameters but also by their probability distributions. In fact, the *probabilistic* nature of hazard maps computed from the invasion frequency within a set of numerical simulations is highly debatable if well-suited calibration procedures are not considered for their construction. For instance, Hyman et al. (2019) showed that selecting a non-uniform distribution over the input range can significantly enhance the robustness of numerical results.

In this section, we describe different strategies to calibrate the input parameters of the energy cone model and box model. To provide a common nomenclature, the calibrated input parameters are named α and β . For the energy cone model, α is defined as the collapse height $H_{0,0}$ and β represents the energy cone slope $\tan(\varphi)$. For the box model, α represents $\log(V_0)$ (with V_0 representing the collapsing volume) and β is defined as the initial particle concentration ϕ_0 . The other input parameters of the box model are fixed. The six inputs of the box model are combined to define only two intermediate variables (L_{max} and C ; see Aravena et al. 2020) which fully define the box model conoids. A calibration based on only two variable parameters is thus enough to capture the variability in the numerical results of this model and to describe the adopted calibration procedures. Our calibration procedures can be eventually generalized to a larger number of variable input parameters. To develop a reproducible calibration procedure, we need to define a similarity index (S) between the results of a set of calibration simulations and a reference scenario or set of reference scenarios. In this work and in the programs ECMapProb 2.0 and BoxMapProb 2.0, the reference scenario (or set of reference scenarios) can be defined in terms of an inundation polygon or in terms of a probability distribution of runout distance or inundation area, which are expected to be based on the geological record of the studied volcano.

Consider a set of $N \times N$ calibration simulations with fixed source position and the input parameters variable within the Cartesian product of predefined ranges ($\alpha \in [\alpha_1, \dots, \alpha_N]$ and $\beta \in [\beta_1, \dots, \beta_N]$). Both sequences of inputs are increasing and their values equidistant. We name $S_{m,n}$ the similarity index between the modeled inundation polygon associated with the m -th value of α and the n -th value of β and the reference scenario or set of reference scenarios. $S_{m,n}$ is assumed to be a non-negative number that increases as the consistency between the modeled inundation polygon and the reference scenario or set of reference scenarios increases. This may translate into a

222 mathematical relationship between $S_{m,n}$ and the sampling probability of the pair of inputs
223 (α_m, β_n) :

$$P((\alpha, \beta) = (\alpha_m, \beta_n)) = c_p \cdot S_{m,n} \quad (1)$$

224 where c_p is a normalizing constant.

225 Considering known values for $S_{m,n}$ we can define a probability function for sampling the model
226 inputs based on the reference scenario or set of reference scenarios. In practice, this means that we
227 can calculate c_p , which is used to normalize the function P to integrate to unity, by assuming:

$$\begin{cases} P(\alpha \in [\alpha_1, \alpha_N]) = 1 \\ P(\beta \in [\beta_1, \beta_N]) = 1 \end{cases} \quad (2)$$

228 In this work we describe five different similarity indexes, which have been implemented in the
229 programs EMapProb 2.0 and BoxMapProb 2.0. Three similarity indexes are based on a reference
230 inundation polygon (i.e., the footprint over the topography of the inundation area of a given PDC;
231 Section 3.1), and the other two similarity indexes are based on predefined probability distributions
232 of runout distance and inundation area, respectively (Section 3.2). These probability distributions
233 are expected to be based on the geological record of the studied volcano.

234 Importantly, all the calibration strategies described in this work consider a possible statistical
235 dependence between the model inputs. In the case of the energy cone model, the well-known
236 relationship between PDC volume and $\tan(\varphi)$ likely translates into a mathematical relationship
237 between $H_{0,0}$ and $\tan(\varphi)$ (see Section 4.1), which would imply that the input parameters cannot
238 be sampled independently for the construction of PDC hazard maps. In the case of the box model,

the product between V_0 and ϕ_0 represents the collapsing volume of pyroclasts, and thus the applicability of an independent sampling is highly debatable (see Section 4.3).

3.1 Metrics based on a reference inundation polygon

Let consider two inundation polygons (A and B) defined by the sets of boundary points A_i and B_j , respectively ($i = 1, \dots, n_a$ and $j = 1, \dots, n_b$). Polygon A is given by the reference inundation area (defined by the user in the programs ECMapProb 2.0 and BoxMapProb 2.0) and polygon B is the result of a given calibration simulation (computed using $\alpha = \alpha_m$ and $\beta = \beta_n$). In our programs, in order to reduce the numerical errors derived from the definition of these polygons and to balance the weight given to the different portions of the polygons, their contour points are re-sampled considering a large number ($n_r = 1,000$) of equidistant points (with respect to the arc length) named A_k and B_k ($k = 1, \dots, n_r$). Below we describe the three different metrics available to calculate $S_{m,n}$ based on a reference inundation polygon (Fig. 2).

3.1.1 Root mean square distance (RMSD)

This similarity index is based on the root mean square distance between the boundary points of each polygon (A_k and B_k) and the closest boundary point of the other one (Fig. 2a), i.e.:

$$RMSD_{m,n} = \frac{\sqrt{\left(\sum_{i=1}^{n_r} \left(\min_{j \in [1, n_r]} \left(d(A_i, B_j) \right)^2 \right) \right) + \left(\sum_{i=1}^{n_r} \left(\min_{j \in [1, n_r]} \left(d(B_i, A_j) \right)^2 \right) \right)}}{2n_r} \quad (3)$$

where $RMSD$ is the 2D-array containing the results of root mean square distance in all the calibration simulations and the subscripts refer to the indices of this matrix. The lower the value

257 of $RMSD_{m,n}$, the higher the similarity degree between the inundation polygons. From these results,
 258 the similarity index can be defined by:

$$S_{m,n}^{(1)} = \left(\frac{1}{RMSD_{m,n} + \varepsilon_{DEM}} \right)^2 \quad (4)$$

259 where ε_{DEM} is the cell size of the DEM used in the calibration simulations, representing a measure
 260 of the DEM resolution-derived uncertainty in the calculation of the distance-based similarity
 261 metrics. We found that the effect of ε_{DEM} was negligible in all the tested cases, but it is still
 262 incorporated in Eq. 4 to avoid division by zero in any simulation condition (note that the minimum
 263 value computed for $RMSD_{m,n}$ in the studied cases is much larger than $\varepsilon_{DEM} \approx 30$ m). In Equation
 264 4 and in all the similarity indexes presented in Section 3.1, we assumed a quadratic relationship to
 265 calculate $S_{m,n}$ in order to enhance the weight of the pairs of input parameters that allow us to
 266 simulate an inundation polygon similar to the reference scenario. The adoption of other
 267 expressions to derive the similarity index from a given comparison metric is also possible (e.g.
 268 Charbonnier et al. 2018; Patra et al. 2020), as well as the inclusion of complementary comparison
 269 metrics.

270 3.1.2 Hausdorff distance (HD)

271 The second similarity index is defined as the maximum distance between a contour point belonging
 272 to one of the inundation polygons and the closest boundary point of the other one (Fig. 2b):

$$HD_{m,n} = \max \left\{ \max_{i \in [1, n_r]} \min_{j \in [1, n_r]} d(A_i, B_j), \max_{i \in [1, n_r]} \min_{j \in [1, n_r]} d(B_i, A_j) \right\} \quad (5)$$

273 where HD is the 2D-array containing the Hausdorff distances associated with all the calibration
274 simulations and the subscripts refer to the indices of this matrix. The associated similarity index
275 can be defined by:

$$S_{m,n}^{(2)} = \left(\frac{1}{HD_{m,n} + \varepsilon_{DEM}} \right)^2 \quad (6)$$

276 where ε_{DEM} is incorporated to avoid division by zero in any simulation condition.

277 **3.1.3 Jaccard index (JI)**

278 This similarity index (Jaccard 1901) compares the areas defined by the inundation polygons, and
279 is given by (Fig. 2c):

$$JI_{m,n} = \frac{|A \cap B|}{|A \cup B|} \quad (7)$$

280 where JI is the 2D-array containing the results of Jaccard index associated with all the calibration
281 simulations and the subscripts refer to the indices of this matrix. The Jaccard index ranges between
282 0 and 1, and its square value is used to derive the associated similarity index (i.e., $S_{m,n}^{(3)} = JI_{m,n}^2$).

283 **3.2 Metrics based on a reference probability distribution of runout distance or inundation** 284 **area**

285 **3.2.1 Runout distance-based calibration**

286 We consider the expected probability distribution of runout distances as a measure potentially
287 useful to calibrate the inputs of PDC numerical models because, in some cases, likely eruption
288 scenarios have been defined by adopting indications on the expected runout distance (e.g. Ferrés
289 et al. 2013). In this case, no reference inundation polygon is needed and calibration is only based

on a predefined distribution of runout distance. If F_{RD} is the cumulative distribution function of runout distance, we can compute a measure of the weight that must be assigned to a calibration simulation characterized by a runout distance $RD_{m,n}$ in order to reproduce the predefined distribution of runout distance:

$$S_{m,n}^{(4)} = \int_0^1 \frac{(|RD_{m,n} - F_{RD}^{-1}(x)| + \varepsilon_{DEM})^{-1}}{\sum_{a=1}^N \sum_{b=1}^N (|RD_{a,b} - F_{RD}^{-1}(x)| + \varepsilon_{DEM})^{-1}} dx \quad (8)$$

where RD is the matrix array containing the runout distances of the calibration simulations, and the subscripts indicate the indices of this matrix. Consider a specific integration step defined by the cumulative probability x_s and thus associated with a specific runout distance $F_{RD}^{-1}(x_s)$. The numerator of Eq. 8 is a measure of the consistency degree between $F_{RD}^{-1}(x_s)$ and $RD_{m,n}$, while the denominator is a normalization factor that considers the consistency degree between $F_{RD}^{-1}(x_s)$ and the runout distance in all the elements of the matrix RD (i.e. all the calibration simulations). ε_{DEM} is incorporated to avoid division by zero in any simulation condition. The cumulative distribution F_{RD} can be any statistical fit of the data, possibly including an extrapolation of extreme events.

3.2.2 Inundation area-based calibration

Finally, because likely eruption scenarios have been also defined using the expected probability distribution of the inundation areas (e.g. Bevilacqua et al. 2017), we also consider the use of this variable to calibrate the input parameters (in this case as well, no reference inundation polygon is needed to develop the calibration simulations). If we define the cumulative distribution function of inundation area by F_{IA} , we can compute the weight that must be assigned to a calibration simulation characterized by the inundation area $IA_{m,n}$ with the aim of reproducing the predefined probability distribution of inundation area:

$$S_{m,n}^{(5)} = \int_0^1 \frac{(|IA_{m,n} - F_{IA}^{-1}(x)| + \varepsilon_{DEM}^2)^{-1}}{\sum_{a=1}^N \sum_{b=1}^N (|IA_{a,b} - F_{IA}^{-1}(x)| + \varepsilon_{DEM}^2)^{-1}} dx \quad (9)$$

where IA is the matrix containing the inundation area of the calibration simulations and the subscripts refer to the indices of this matrix. The reason for including ε_{DEM}^2 is equivalent to that presented previously.

In ECMapProb 2.0 and BoxMapProb 2.0, the number of simulations to be performed in the calibration step is defined by the user. However, in order to mitigate discretization errors, the comparison metrics (i.e. $RMSD$, HD , JI , RD and IA) are interpolated in the input space, giving rise to a sufficiently large matrix, which considers $N = 100$ and preserves the limits of the ranges defined by the user for α and β . As an alternative to the described calibration strategies, our programs also allow the user to define *a priori* the probability distributions adopted to sample the input parameters. Various options are available to set the vent position as well, including pointwise, linear and radial geometries or a set of positions expressly defined by the user, which can be flexibly adopted for testing the influence of collapse position in PDC propagation.

4. Test cases: results and discussion

Here we present three applications of our calibration strategies and their discussion. El Misti volcano (Peru) was adopted to show the use of calibrations based on a reference inundation polygon for constructing probability maps of PDC inundation; Merapi volcano (Indonesia) was adopted to illustrate the use of calibrations based on the expected distribution of runout distance; while Campi Flegrei (Italy) was selected to show the use of calibrations based on the expected distribution of inundation area, also exemplifying the effects of several sources of data uncertainty. Since the reference scenario adopted for El Misti includes both valley-confined deposits and over bank deposits on the valley margins (Charbonnier et al. 2020), the concomitance of dense and

dilute PDCs is likely. For simplicity, we limit our analysis of El Misti to the use of the branching energy cone model, which is expected to better describe dense gravity-driven PDCs. Because most of the PDCs generated at Merapi volcano are derived from dome collapses (i.e. they are frictional flows), we used the branching energy cone model. Finally, since Campi Flegrei eruptions tend to produce dilute, inertial PDCs, they are better described by the box model (Esposti Ongaro et al. 2016). In the latter case, we adopted the traditional formulation instead of the branching one because minor channelization processes are expected in such a flat topography and because this choice allows us to perform comparisons with the most recent PDC hazard assessments at Campi Flegrei (Neri et al. 2015b; Bevilacqua et al. 2017). Additionally, in this test case we set vent position by coupling the box model with vent opening probability maps (Bevilacqua et al., 2021).

4.1 El Misti volcano

El Misti volcano (5,822 m a.s.l.) is located 13 km NE of Arequipa city (>1 million inhabitants, at an altitude 3,500 m lower than the summit of El Misti). These factors and its potential to develop PDC-forming eruptions (Legros 2001; Thouret et al. 2001; Harpel et al. 2011; Sandri et al. 2014; Charbonnier et al. 2020) justify the use of this volcano as a case study for illustrating the application of our calibration strategies. In fact, at least three sub-Plinian and Plinian eruptions occurred at El Misti during the last 10,000 years, intercalated with small-magnitude Vulcanian events (Cobeñas et al. 2012). Following Cobeñas et al. (2012) and Charbonnier et al. (2020), we use the 2070 cal yr BP Plinian eruption as a reference event to assess PDC hazard at El Misti volcano, which corresponds to a VEI 4 event for which the recurrence rate has been estimated between 2000 and 4000 years (Charbonnier et al. 2020). Presentation of updated hazard maps is beyond the objectives of this work (for which the reader can consult the official hazard map for El Misti; Mariño et al. 2008); we aim instead at presenting an illustrative application of our calibration

strategies. For this, we used the inundation polygon of the PDCs derived from the 2070 cal yr BP Plinian eruption (Fig. 3a; Charbonnier et al. 2020) to calibrate the input parameters of the branching energy cone model, considering a fixed collapse position at the summit crater (Fig. 3a), $H_{0,0}$ from 100 m to 2,000 m, and $\tan(\varphi)$ ranging between 0.2 and 1.0.

We performed 400 calibration simulations using the program EMapProb 2.0. Figure 3b-d shows the pseudo-color plots derived from the calibration simulations, based on the following metrics: RMSD, HD and JI. This figure highlights the strong correlation between $H_{0,0}$ and $\tan(\varphi)$ in determining the different similarity indexes. Calibration results were then used to sample three sets of input parameters, each one derived from the application of a different metric (RMSD, HD and JI, respectively; Fig. 3e-g). With this information, we performed three additional sets of simulations aimed at constructing scenario-based probability maps of PDC inundation. Here we also introduced a small variability in vent position, which was sampled uniformly within a 200 m-radius circle centered in the collapse position used in the calibration simulations (Fig. 3a).

The resulting probability maps of PDC inundation (Fig. 4) are highly consistent with each other and with Cobeñas et al. (2012) and Sandri et al. (2014). They show a preferential propagation direction toward SW (i.e., toward the basin and the city of Arequipa, reaching in many cases its suburbs). Runout distance typically ranges between 6 km and 15-17 km (mean value of about 10 km and median value of ~9 km; Fig. 4 and supplementary Table C1). The branching energy cone model predicts non-negligible channelization processes through Chili River, which agrees with the geological record at El Misti volcano and influences the inundation probability in the northern portion of Arequipa (Fig. 4). Significant channelization processes toward NE and SE are not apparent in the numerical results. Figure 4 shows that the 50% isolines of the resulting probabilistic maps tend to present a behavior similar to the reference scenario (indicated by a green line in Fig.

4), but it presents shorter propagation distances in the channelization zones. However, the 10% isolines envelope most of the inundation area of the reference scenario also in the channelization domains.

Importantly, channelization through the San Lázaro catchment is significant at proximal and medial zones and small at distal domains, and very weak channelization is modelled along the Huarangal catchment. This is apparently inconsistent with Charbonnier et al. (2020), who recognized these catchments as relevant for the channelization of pyroclastic material to Arequipa. Our simulations were calibrated using a specific reference deposit with very limited channelization through these catchments and, more importantly, our collapse positions are located in the summit zone, while the simulations performed by Charbonnier et al. (2020) were developed considering the collapse of already channelized pyroclastic material (the collapsing material was initially located at the apex of two specific drainage networks, at >2 km from the summit crater). Consequently, as Charbonnier et al. (2020) indicate, their probabilistic maps are not only conditioned on the occurrence of a VEI 4 eruption, but also on the entrance of large volumes of pyroclastic material in two specific drainage networks that threaten Arequipa; while our probabilistic maps are conditioned exclusively on the occurrence of an event similar to the 2070 cal yr BP Plinian eruption. These differences in the objectives and thus in the criteria adopted in the calibration step hinder the development of further comparisons with Charbonnier et al. (2020), and highlight the necessity of considering separately the PDCs initiated from the summit and near the drainage networks at El Misti volcano. In any case, to show that this difference derives from the adoption of different calibration criteria instead of limitations of the branching energy cone model to channelize pyroclastic material, we performed additional simulations with a vent located on the flanks of the volcano, which are displayed in the supplementary Figure C1. These

simulations show the potential of the branching energy cone model to predict highly channelized flows along the main drainage networks of El Misti volcano.

In this section we adopted three different metrics to construct independent probabilistic maps of PDC inundation. The definition of a *preferred* calibration metric is likely controlled by the specific case study and model adopted, and thus providing general considerations is not straightforward. We suggest, however, that calibration metrics based on the inundation area contour (e.g. Hausdorff distance and RMSD) are probably more appropriate than the Jaccard Index when we study volcanoes that have presented intense channelization along valleys, or when this process is particularly critical for risk assessment. In any case, the construction of independent probability maps can be useful to define uncertainty ranges in the resulting hazard maps.

4.2 Merapi volcano

Merapi stratovolcano (~2,930 m a.s.l.) is located ~25 km north of the metropolitan area of Yogyakarta, Central Java, Indonesia. This volcano has experienced frequent dome-forming activity during the last centuries able to generate PDCs (“*Merapi-type*” *nuées ardentes*) and subsequent lahars (Boudon et al. 1993; Voight et al. 2000; Voight and Davis 2000; Bourdier and Abdurachman 2001; Thouret et al. 2001; Lube et al. 2011; Gertisser et al. 2012; Surono et al. 2012; Charbonnier et al. 2013; Komorowski et al. 2013; Kelfoun et al. 2021). The topography of Merapi, characterized by numerous radial valleys, has exerted a significant effect in the propagation of PDCs, and also the crater configuration and collapse position have influenced the transport direction of recent PDCs (e.g. Charbonnier and Gertisser 2008). For instance, because of the topographic barriers present at the NE of the volcano summit, most of the recent PDCs propagated towards S, SW and W (Solikhin 2015).

The dynamics of this type of PDC is dominated by gravitational acceleration on the volcanic slopes and granular frictional dissipation, making them suitable for the use of the branching energy cone model. The presentation of new hazard maps is beyond the objectives of this article, for which the reader can consult the wide volcanological literature at Merapi (Andreastuti et al. 2000; Itoh et al. 2000; Lavigne et al. 2000; Thouret et al. 2000; Charbonnier and Gertisser 2009; Charbonnier and Gertisser 2012; Mei et al. 2013; Lavigne et al. 2015; Kelfoun et al. 2017) and the official hazard map of this volcano (Sayudi et al. 2010).

The availability of detailed information about the dispersion of PDCs in the past (e.g. Bourdier and Abdurachman 2001; Solikhin 2015) allows us to consider the expected distribution of runout distance to calibrate our numerical model. To do this, first we performed 400 calibration simulations using the branching energy cone model and considering a fixed collapse position at the summit crater, $H_{0,0}$ ranging from 40 m to 200 m, and $\tan(\varphi)$ ranging between 0.2 and 1.0. The small range adopted for $H_{0,0}$ is justified by the generation mechanism of most of the PDCs at Merapi, i.e. dome collapse. Figure 5a-b presents the pseudo-color plots of runout distance and inundation area in the calibration simulations. Because of the high slope that characterizes the volcano flanks in the proximal area ($>30^\circ$), a significant gap is observed in the simulated runout distances between ~ 0.2 km (i.e. inside the crater limits) and ~ 2.5 km (Fig. 5a). In other words, all the simulations that exceeded the crater limits were able to travel at least ~ 2.5 km from the source due to the high slopes encountered by the PDC in this zone of the volcano.

To define the input probability distribution of runout distance, we adopted the information summarized by Solikhin (2015), who compiled the runout distances of 55 PDCs between 1900 and 2010 (Fig. 5c-d). In particular, the runout distances of these events were fitted considering both gamma and lognormal probability functions (Fig. 5c-d). Although a bimodal distribution could be

hypothesized to describe the data, we decided to keep the discussion simpler and focus on the calibration features. The coupling of calibration simulations and the two predefined distributions of runout distance give rise to two sampling probability distributions of input parameters (Figure 5e-f), which were then used in two sets of 500 simulations to construct PDC inundation probability maps. This number of simulations is large enough for the probability maps to converge. To carry out these simulations, collapse positions were sampled uniformly from a 300 m-radius circle centered in the collapse position used for the calibration simulations (i.e. the volcano summit).

The resulting inundation maps are displayed in Figure 6. Even though we sampled the collapse positions uniformly, results reproduce well the preferential propagation directions observed at Merapi volcano (i.e. S, W, NW and SW), which are also observed in hazard maps derived from the geological record of Merapi volcano (e.g. Figure 4 of Thouret et al. 2000). The small inundation probabilities simulated at distances of the order of 15 km, which are present in the geological record of Merapi (Newhall et al. 2000), are consequences of the limited dataset adopted in the numerical calibration (i.e. PDCs between 1900 and 2010), which implies that our probability maps are conditioned on the occurrence of an eruption that follows the eruption variability of the last century (Solikhin 2015).

Differences between the results associated with the gamma and lognormal fits are negligible (Fig. 6, Fig. 7a and supplementary Table C2). In these simulations, mean runout distance is 5.8-5.9 km, with 90% confidence intervals of [3.2, 12.1] km and [3.1, 11.5] km for the results associated with gamma and lognormal fits, respectively (supplementary Table C2). The branching energy cone model predicts non-negligible channelization processes through different river valleys such as Senowo, Apu, Woro, Opak and Gendol, which agrees with the recent activity at Merapi volcano (Fig. 6). Interestingly, although the last major PDC at Merapi was channelized through the Gendol

catchment, our results suggest a dominant channelization effect of Woro and Opak catchments to the south. This apparent inconsistency with the last eruption is instead coherent with the geological record of the last century (Solikhin 2015).

Figure 7 presents the comparison between the CDFs of the predefined distributions of runout distance, which derive from two fits based on the geological record of Merapi (gamma and lognormal; dashed lines), and the resulting distributions of runout distance in the simulations presented in Figure 6 (continuous lines). The empirical CDF of 55 documented PDCs is also included (Solikhin 2015). The main contrast between the predefined and resulting CDFs derives from the absence of simulations with runout distances lower than 2.5 km. We speculate that low-runout distance PDCs observed at Merapi can be related to volume-limited block-and-ash flows (or simply a rock-fall rather than a PDC), whose dynamics cannot be modeled by the branching energy cone model. The presence of different families of PDCs at Merapi could be responsible for the bimodal behavior of documented runout distances (Fig. 5c-d). Additional differences between the predefined and resulting CDFs presented in Figure 7 may derive from the use of a calibration based on simulations performed using a single collapse position, while a small uncertainty in collapse position was introduced for the construction of the hazard maps presented in Figure 6. Since a major challenge to evaluate the hazard associated with dome collapse at Merapi is the frequent occurrence of changes in the eruption site (Thouret et al. 2000), in the Supplementary Figure C2 we show the results of four sets of simulations with collapse positions at different regions of the volcano summit. These results stress that small differences in the collapse position (e.g. of the order of hundreds of meters) are able to change dramatically the expected propagation of PDCs and the valleys involved.

Note that these maps are conditioned on the occurrence of a PDC derived from the collapse of a summit dome, which is not the only mechanism able to produce PDCs at Merapi. In fact, this volcano has presented large explosive eruptions in historic times, such as the 1872 eruption (Hartmann 1934).

4.3 Campi Flegrei

Campi Flegrei, located on the Campanian plain in Southern Italy, is a 12 km wide caldera that includes a highly urbanized area and a significant portion of the city of Naples. The volcanic activity of Campi Flegrei during the last 15 kyr has been separated in three epochs of temporally clustered eruptions, which include at least 70 explosive events (e.g. Di Vito et al. 1999; Smith et al. 2011; Bevilacqua et al. 2016; Isaia et al. 2019). Among the products of these eruptions, PDCs represent the main volcanic hazard (Lirer et al. 2001; Alberico et al. 2002; 2011; Orsi et al. 2004; 2009; Rossano et al. 2004; Todesco et al. 2006; Neri et al. 2015b; Tierz et al. 2016b; Bevilacqua et al. 2017) but their assessment is particularly challenging due to the large uncertainty in the position of future vents (Alberico et al. 2002; Orsi et al. 2004; Selva et al. 2012; Bevilacqua et al. 2015; 2017; 2020; Rivalta et al. 2019).

The availability of detailed information about the dispersion of PDCs in the past allows us to consider the expected distribution of inundation area to calibrate the box model. To do this, we performed two sets of 900 calibration simulations each by adopting the traditional formulation of the box model, with the collapsing volume ranging from 10^6 to 10^{11} m³ and the initial concentration of solid particles between 0.5 vol. % and 4.0 vol. %. The range adopted for the collapsing volume spans over several orders of magnitude (including the best-fit range with the inundation areas of documented PDCs, as observed below), while the values adopted for the initial concentration of solid particles are those expected for dilute PDCs. The other input parameters of the box model

were fixed (sedimentation velocity of 0.6 m/s, Froude number of 1.1, pyroclasts density of 1500 kg/m³ and ambient gas density of 1.1 kg/m³). Note that the number of calibration simulations is sensibly larger than those adopted in previous sections due to the different variation ranges of the input parameters. For Campi Flegrei simulations, considering that the collapsing volume ranges over five orders of magnitude, a large number of simulations is needed to produce smooth sampling probability distributions for the model inputs. Both sets of calibration simulations for Campi Flegrei differ in the collapse position, set at Monte Nuovo and Agnano, respectively (Fig. 8a), and allow us to calculate the inundation area as a function of the two variable input parameters (Fig. 8b-c). Although the uncertainty in vent position in this volcanic field may raise doubts about the use of a fixed vent position for calibration purposes, the absence of major topographic barriers at Campi Flegrei (with the exception of the caldera rim, ~160 m high, or the rim of the Agnano plain, ~110 m high) produces only small differences in the calibration results as a function of the collapse position. In particular, we adopted the calibration data of Monte Nuovo and Agnano as representative for the western and eastern sectors of Campi Flegrei, respectively. In the following we further evaluate the validity of this assumption.

Because the calibration procedure described in Section 3.2.2 needs the input of a probability distribution of inundation area, we used the information summarized by Neri et al. (2015b), which relies largely on Orsi et al. (2004). In particular, we followed the strategy of Neri et al. (2015b) and Bevilacqua et al. (2017) to consider the variability of inundation area in 47 documented PDCs, the effect of possible underestimations of the area of PDC deposits, and the presence of “lost” deposits in the dataset. Therefore, we provided an example of the effect of data uncertainty on our calibration algorithm, besides the model uncertainty (Kennedy and O’Hagan 2001; Bayarri et al. 2007a; 2007b). Furthermore, we considered the western and eastern domains of Campi Flegrei

separately because significant differences have been recognized in the typical scale of their eruptions (for additional details, see Bevilacqua et al. 2017). This allowed us to define the expected distribution of inundation area in the two regions of Campi Flegrei, which are displayed as cumulative curves in Figure 8d-e. These results show that the inundation area of a PDC generated at the eastern sector of Campi Flegrei tends to be significantly larger than that expected in the western portion of this volcanic field.

The coupling of the calibration simulations (Fig. 8b-c) and the expected distributions of inundation area (Fig. 8d-e) gives rise to two sampling probability distributions of input parameters, which are displayed in Figure 9. These results show a strong correlation between the two input parameters in the calculation of the calibration similarity indexes, suggesting that interdependent sampling strategies of the model inputs should be preferred (Fig. 9). As expected, the peak of sampling probability for the western sector of Campi Flegrei (computed for collapsing volumes of $V_0 = 10^7 - 3 \cdot 10^8 \text{ m}^3$) is associated with much smaller PDCs than that predicted for the eastern zone of this caldera (computed for collapsing volumes of $V_0 = 3 \cdot 10^8 - 2 \cdot 10^9 \text{ m}^3$), with differences of one order of magnitude (Fig. 9).

With this information, we performed two sets of 3,000 simulations to construct PDC inundation probability maps for the two sectors of Campi Flegrei. To carry out these simulations, collapse positions were sampled using the vent opening probability map presented by Bevilacqua et al. (2015). Note that this map includes uncertainty ranges but, for simplicity, in this work we adopted the mean value map. We also discarded all the vents located offshore and considered separately the western and eastern sectors of Campi Flegrei (using the limits adopted by Bevilacqua et al. 2017). On the other hand, following Bevilacqua et al. (2017), the sea surface has been considered as a flat topography with no consideration of water influence on the PDC propagation dynamics.

Numerical results, visualized in a GIS environment, are displayed in Figure 10a-b. We remark that these maps are conditioned on the occurrence of a PDC-forming eruption in the western and eastern sectors of Campi Flegrei, respectively. We also include the combined probabilistic map of PDC inundation (Fig. 10c), defined using the relative weights of the two sectors of Campi Flegrei in the vent opening maps of Bevilacqua et al. (2015), i.e. 30.7% for the western sector and 69.3% for the eastern sector. For an eruption located in the western sector of Campi Flegrei, our simulations show a peak of PDC inundation probability of about 30% at Averno, being strongly consistent with Bevilacqua et al. (2017). For an eruption located in the eastern portion of this volcanic system, numerical results show a maximum PDC inundation probability of ~60% at Astroni and Agnano, with probabilities around 15-20% of having a PDC able to overcome the Posillipo Hill, again in agreement with the results presented by Bevilacqua et al. (2017). Differences in the maximum values of PDC inundation probability between the two sectors of Campi Flegrei are mainly derived from the scale of the PDCs expected, which are much larger in the eastern sector. The combined probability map of PDC inundation, which is not conditioned on the sector of the source position, presents a maximum value of ~43% at Agnano and Astroni, and a probability of ~10-15% of overcoming the Posillipo Hill. The consistency between our results and Bevilacqua et al. (2017) can be considered an expected result because we used the same geological dataset to calibrate the models. However, we stress that the calibration procedures are completely different.

Finally, Figure 11 presents the comparison between the CDFs of the predefined distributions of inundation area (continuous red lines) and the resulting distributions of this variable in the simulations presented in Figure 10a-b (dashed blue lines). The empirical CDF of inundation area in the geological record of Campi Flegrei is also displayed (black line). The strong agreement

between the prescribed and the resulting distributions of inundation area confirms that a calibration procedure based on simulations performed using a single source point is able to capture well the dependence between the box model input parameters and the resulting inundation area in this volcanic system, where the topographic roughness is small.

5. Summary and conclusions

Although numerical models have become a fundamental tool in the assessment of volcanic hazard and in the design of volcanic risk mitigation strategies (e.g. Ferrés et al. 2013; Sandri et al. 2014; Bevilacqua et al. 2017; Charbonnier et al. 2020; Clarke et al. 2020; Esposti Ongaro et al. 2020b), the large variety of criteria used to define their input parameters often limits the development of comparisons between different numerical models, which is a critical step for their validation (Esposti Ongaro et al. 2020a). In this work, we propose a set of structured and reproducible procedures to calibrate the input parameters of PDC numerical models, which are based on the characteristics of past PDCs in the studied volcanic system. These can be described in terms of:

(a) A reference inundation map (described as a polygon) from a specific eruption. Three parameters to compute the similarity index between this polygon and a set of calibration simulations have been considered (RMSD, Hausdorff distance, and Jaccard Index). Calibration simulations results can be used to define different sampling probability distributions of the input parameters, which in turn can be adopted to extract a set of calibrated inputs to use in numerical simulations. The application of these calibrations enables the construction of probabilistic maps of PDC inundation conditioned on the occurrence of an event similar to the reference scenario (i.e. scenario-based hazard assessment, see Section 4.1). Moreover, the parallel use of different metrics allows us to construct independent probability maps, potentially useful to define uncertainty ranges in the resulting hazard maps.

(b) The distribution of runout distances or inundation area of past PDCs. This information, along with the results of the calibration simulations, allow us to sample a set of input parameters able to reflect the eruptive history of the volcano. These two procedures, whose application involves a large knowledge of the characteristics of the studied volcanic system, are able to produce PDC inundation probabilistic maps conditioned on the occurrence of a PDC-forming eruption without assumptions associated with its characteristics (e.g. magnitude or intensity, see Sections 4.2 and 4.3).

The suitability of the different calibration procedures will be naturally controlled by the availability of detailed information of the studied volcanic system and by the approach used to assess the hazard derived from PDCs (e.g. based on a specific scenario or not). These strategies consider the interaction of the input parameters in controlling the numerical results (in other words, input parameters are not sampled independently). All the tested cases exhibit a strong interdependence between the input parameters in the resulting functions of sampling probability, suggesting that calibration strategies that consider interdependent sampling should be preferred for the construction of probabilistic maps of PDC inundation. In fact, our approach produces multivariate probability density functions over the input space rather than optimal input values. This is particularly important when dealing with very uncertain conditions, and possible data inadequacy or model inaccuracy (Kennedy and O'Hagan 2001; Bayarri et al. 2007a, 2007b). We remark that our approach can deal with both data uncertainty and the statistical extrapolation of extreme events.

We have illustrated our calibration strategies by applying them to three volcanoes: El Misti, Merapi and Campi Flegrei. In general terms, results are strongly consistent with previous hazard assessments and with the geological record of these volcanic systems (e.g., Cobeñas et al. 2012; Sandri et al. 2014; Neri et al. 2015b; Solikhin 2015; Bevilacqua et al. 2017). In any case, our results

are not intended to represent updated hazard maps of these well-documented volcanoes, for which the reader should consult the official maps and other recent studies of volcanic hazard (e.g. Mariño et al. 2008; Sayudi et al. 2010; Sandri et al. 2014; Neri et al. 2015b; Bevilacqua et al. 2017; Charbonnier et al. 2020).

The different calibration procedures described here were implemented on improved, user-friendly versions of the programs EMapProb 2.0 and BoxMapProb 2.0, whose functionalities and user manuals are presented for the first time in this article (see Supplementary material). These open-source and freely downloadable programs adopt the traditional and branching formulations of the energy cone and the box model (Aravena et al., 2020), respectively, and thus they present different applicability fields (frictional and inertial flows, respectively).

Code availability

EMapProb 2.0 is available in <https://github.com/AlvaroAravena/EMapProb> (Apache 2.0 license). BoxMapProb 2.0 is available in <https://github.com/AlvaroAravena/BoxMapProb> (Apache 2.0 license).

Acknowledgement

We appreciate the systematic compilation of volcanological data presented by Dr. A. Solikhin in his doctoral thesis, which was strongly useful for one of the applications presented here. We thank Dr. Greg Valentine and two anonymous reviewers for their useful comments and suggestions. Alvaro Aravena was financed by the French government IDEX-ISITE initiative 16-IDEX-0001 (CAP 20-25).

References

649 Alberico I, Lirer L, Petrosino P, Scandone R (2002) A methodology for the evaluation of long-
 650 term volcanic risk from pyroclastic flows in Campi Flegrei (Italy). *Journal of Volcanology and*
 651 *Geothermal Research* 116(1-2):63-78. [https://doi.org/10.1016/S0377-0273\(02\)00211-1](https://doi.org/10.1016/S0377-0273(02)00211-1)

652 Alberico I, Petrosino P, Lirer L (2011) Volcanic hazard and risk assessment in a multi-source
 653 volcanic area: the example of Napoli city (Southern Italy). *Natural Hazards and Earth System*
 654 *Sciences* 11:1057-1070. <https://doi.org/10.5194/nhess-11-1057-2011>

655 Anderson KR, Johanson IA, Patrick MR, Gu M, Segall P, Poland MP, Montgomery-Brown EK,
 656 Miklius A (2019) Magma reservoir failure and the onset of caldera collapse at Kīlauea Volcano in
 657 2018. *Science* 366(6470). <https://doi.org/10.1126/science.aaz1822>

658 Andreastuti SD, Alloway BV, Smith IEM (2000) A detailed tephrostratigraphic framework at
 659 Merapi Volcano, Central Java, Indonesia: implications for eruption predictions and hazard
 660 assessment. *Journal of Volcanology and Geothermal Research* 100(1-4):51-67.
 661 [https://doi.org/10.1016/S0377-0273\(00\)00133-5](https://doi.org/10.1016/S0377-0273(00)00133-5)

662 Aravena A, Cioni R, Bevilacqua A, de' Michieli Vitturi M, Esposti Ongaro T, Neri A (2020) Tree-
 663 branching- based enhancement of kinetic energy models for reproducing channelization processes
 664 of pyroclastic density currents. *Journal of Geophysical Research: Solid Earth*
 665 125(7):e2019JB019271. <https://doi.org/10.1029/2019JB019271>

666 Asmussen S, Hering H (1983) *Branching processes*. Springer. [https://doi.org/10.1007/978-1-4615-](https://doi.org/10.1007/978-1-4615-8155-0)
 667 [8155-0](https://doi.org/10.1007/978-1-4615-8155-0)

668 Aspinall W, Woo G (2019) Counterfactual analysis of runaway volcanic explosions. *Frontiers in*
 669 *Earth Science* 7:222. <https://doi.org/10.3389/feart.2019.00222>

670 Bartolini S, Martí J, Sobradelo R, Becerril L (2017) Probabilistic e-tools for hazard assessment
671 and risk management. In: Volcanic Unrest (pp. 47-61). Springer, Cham.
672 https://doi.org/10.1007/11157_2017_14

673 Bayarri MJ, Berger JO, Paulo R, Sacks J, Cafeo JA, Cavendish J, Lin CH, Tu J (2007a) A
674 framework for validation of computer models. *Technometrics* 49(2):138-154.
675 <https://doi.org/10.1198/004017007000000092>

676 Bayarri MJ, Walsh D, Berger JO, Cafeo J, Garcia-Donato G, Liu F, Palomo J, Parthasarathy RJ,
677 Paulo R, Sacks J (2007b) Computer model validation with functional output. *The Annals of*
678 *Statistics* 35(5):1874-1906. <https://doi.org/10.1214/009053607000000163>

679 Bayarri MJ, Berger JO, Calder ES, Dalbey K, Lunagomez S, Patra AK, Pitman EB, Spiller ET
680 (2009) Using statistical and computer models to quantify volcanic hazards. *Technometrics*
681 51(4):402–413. <https://doi.org/10.1198/TECH.2009.08018>

682 Bayarri MJ, Berger JO, Calder ES, Patra A, Pitman EB, Spiller ET, Wolpert RL (2015)
683 Probabilistic quantification of hazards: a methodology using small ensembles of physics-based
684 simulations and statistical surrogates. *International Journal for Uncertainty Quantification* 5(4).
685 <https://doi.org/10.1615/Int.J.UncertaintyQuantification.2015011451>

686 Bevilacqua A (2016) Doubly stochastic models for volcanic hazard assessment at Campi Flegrei
687 caldera. Springer. <https://doi.org/10.1007/978-88-7642-577-6>

688 Bevilacqua A, Aravena A, Neri A, Gutiérrez E, Escobar D, Schliz M, Aiuppa A, Cioni R (2021)
689 Thematic vent opening probability maps and hazard assessment of small-scale pyroclastic density
690 currents in the San Salvador volcanic complex (El Salvador) and Nejapa-Chiltepe volcanic

691 complex (Nicaragua). *Natural Hazards and Earth System Sciences* 21:1639–1665.
692 <https://doi.org/10.5194/nhess-21-1639-2021>

693 Bevilacqua A, Flandoli F, Neri A, Isaia R, Vitale S (2016) Temporal models for the episodic
694 volcanism of Campi Flegrei caldera (Italy) with uncertainty quantification. *Journal of Geophysical*
695 *Research: Solid Earth* 121(11):7821–7845. <https://doi.org/10.1002/2016JB013171>

696 Bevilacqua A, Isaia R, Neri A, Vitale S, Aspinall W, Bisson M, Flandoli F, Baxter P, Bertagnini
697 A, Esposti Ongaro T (2015) Quantifying volcanic hazard at Campi Flegrei caldera (Italy) with
698 uncertainty assessment: 1. Vent opening maps. *Journal of Geophysical Research: Solid Earth*
699 120(4):2309–2329. <https://doi.org/10.1002/2014JB011775>

700 Bevilacqua A, Neri A, Bisson M, Esposti Ongaro T, Flandoli F, Isaia R, Rosi M, Vitale S (2017)
701 The effects of vent location, event scale, and time forecasts on pyroclastic density current hazard
702 maps at Campi Flegrei caldera (Italy). *Frontiers in Earth Science* 5:72.
703 <https://doi.org/10.3389/feart.2017.00072>

704 Bevilacqua A, Neri A, De Martino P, Isaia R, Novellino A, Tramparulo F, Vitale S (2020) Radial
705 interpolation of GPS and leveling data of ground deformation in a resurgent caldera: application
706 to Campi Flegrei (Italy). *Journal of Geodesy* 94(2):1–27. [https://doi.org/10.1007/s00190-020-](https://doi.org/10.1007/s00190-020-01355-x)
707 [01355-x](https://doi.org/10.1007/s00190-020-01355-x)

708 Bevilacqua A, Patra AK, Bursik MI, Pitman EB, Macías JL, Saucedo R, Hyman D (2019)
709 Probabilistic forecasting of plausible debris flows from Nevado de Colima (Mexico) using data
710 from the Atenquique debris flow, 1955. *Natural Hazard and Earth System Sciences* 19:791–820.
711 <https://doi.org/10.5194/nhess-19-791-2019>

712 Biass S, Bonadonna C, Connor L, Connor C (2016) TephraProb: a Matlab package for probabilistic
713 hazard assessments of tephra fallout. *Journal of Applied Volcanology* 5:10.
714 <https://doi.org/10.1186/s13617-016-0050-5>

715 Boudon G, Camus G, Gourgaud A, Lajoie J (1993) The 1984 nuée-ardente deposits of Merapi
716 volcano, Central Java, Indonesia: stratigraphy, textural characteristics, and transport mechanisms.
717 *Bulletin of Volcanology* 55(5):327-342. <https://doi.org/10.1007/BF00301144>

718 Bourdier JL, Abdurachman E (2001) Decoupling of small-volume pyroclastic flows and related
719 hazards at Merapi volcano, Indonesia. *Bulletin of Volcanology* 63:309-325.
720 <https://doi.org/10.1007/s004450100133>

721 Campbell CS (2006) Granular material flows—an overview. *Powder Technology* 162(3):208-229.
722 <https://doi.org/10.1016/j.powtec.2005.12.008>

723 Charbonnier S, Connor C, Connor L, Sheridan M, Hernández J, Richardson J (2018) Modeling the
724 October 2005 lahars at Panabaj (Guatemala). *Bulletin of Volcanology* 80:1-16.
725 <https://doi.org/10.1007/s00445-017-1169-x>

726 Charbonnier S, Germa A, Connor CB, Gertisser R, Preece K, Komorowski JC, Lavigne F, Dixon
727 T, Connor L (2013) Evaluation of the impact of the 2010 pyroclastic density currents at Merapi
728 volcano from high-resolution satellite imagery, field investigations and numerical simulations.
729 *Journal of Volcanology and Geothermal Research* 261:295-315.
730 <https://doi.org/10.1016/j.jvolgeores.2012.12.021>

731 Charbonnier S, Gertisser R (2008) Field observations and surface characteristics of pristine block-
732 and-ash flow deposits from the 2006 eruption of Merapi Volcano, Java, Indonesia. *Journal of*

733 Volcanology and Geothermal Research 177(4):971-982.
734 <https://doi.org/10.1016/j.jvolgeores.2008.07.008>

735 Charbonnier S, Gertisser R (2009) Numerical simulations of block-and-ash flows using the
736 Titan2D flow model: examples from the 2006 eruption of Merapi Volcano, Java, Indonesia.
737 Bulletin of Volcanology 71:953–959. <https://doi.org/10.1007/s00445-009-0299-1>

738 Charbonnier S, Gertisser R (2012) Evaluation of geophysical mass flow models using the 2006
739 block-and-ash flows of Merapi Volcano, Java, Indonesia: Towards a short-term hazard assessment
740 tool. Journal of Volcanology and Geothermal Research 231-232:87-108.
741 <https://doi.org/10.1016/j.jvolgeores.2012.02.015>

742 Charbonnier S, Thouret JC, Gueugneau V, Constantinescu R (2020) New insights into the 2070
743 cal yr BP pyroclastic currents at El Misti volcano (Peru) from field investigations, satellite imagery
744 and probabilistic modeling. Frontiers in Earth Science 8:398.
745 <https://doi.org/10.3389/feart.2020.557788>

746 Cioni R, Tadini A, Gurioli L, Bertagnini A, Mulas M, Bevilacqua A, Neri A (2020) Estimating
747 eruptive parameters and related uncertainties for pyroclastic density currents deposits: worked
748 examples from Somma-Vesuvius (Italy). Bulletin of Volcanology 82(9):1-20.
749 <https://doi.org/10.1007/s00445-020-01402-7>

750 Clarke B, Tierz P, Calder E, Yirgu G (2020) Probabilistic volcanic hazard assessment for
751 pyroclastic density currents from pumice cone eruptions at Aluto volcano, Ethiopia. Frontiers in
752 Earth Science 348. <https://doi.org/10.3389/feart.2020.00348>

753 Cobeñas G, Thouret JC, Bonadonna C, Boivin P (2012) The c. 2030 yr BP Plinian eruption of El
 754 Misti volcano, Peru: eruption dynamics and hazard implications. *Journal of Volcanology and*
 755 *Geothermal Research* 241-242:105-120. <https://doi.org/10.1016/j.jvolgeores.2012.06.006>
 756 Dalbey K, Patra AK, Pitman EB, Bursik MI, Sheridan MF (2008) Input uncertainty propagation
 757 methods and hazard mapping of geophysical mass flows. *Journal of Geophysical Research*
 758 113:B05203. <https://doi.org/10.1029/2006JB004471>
 759 de' Michieli Vitturi M, Esposti Ongaro T, Lari G, Aravena A (2019) IMEX_SfloW2D 1.0: a depth-
 760 averaged numerical flow model for pyroclastic avalanches. *Geoscientific Model Development*
 761 12:581-595. <https://doi.org/10.5194/gmd-12-581-2019>
 762 de' Michieli Vitturi M, Tarquini S (2018) MrLavaLoba: A new probabilistic model for the
 763 simulation of lava flows as a settling process. *Journal of Volcanology and Geothermal Research*
 764 349:323-334. <https://doi.org/10.1016/j.jvolgeores.2017.11.016>
 765 Di Vito MA, Isaia R, Orsi G, Southon J, De Vita S, D'Antonio M, Pappalardo L, Piochi M (1999)
 766 Volcanism and deformation since 12,000 years at the Campi Flegrei caldera (Italy). *Journal of*
 767 *Volcanology and Geothermal Research* 91(2-4):221-246. [https://doi.org/10.1016/S0377-](https://doi.org/10.1016/S0377-0273(99)00037-2)
 768 [0273\(99\)00037-2](https://doi.org/10.1016/S0377-0273(99)00037-2)
 769 Doyle EE, Hogg AJ, Mader HM, Sparks RSJ (2010) A two-layer model for the evolution and
 770 propagation of dense and dilute regions of pyroclastic currents. *Journal of Volcanology and*
 771 *Geothermal Research* 190(3-4):365-378. <https://doi.org/10.1016/j.jvolgeores.2009.12.004>
 772 Druitt TH (1998) Pyroclastic density currents. Geological Society, London, Special Publications
 773 145(1):145-182. <https://doi.org/10.1144/GSL.SP.1996.145.01.08>

774 Dufek J, Esposti Ongaro T, Roche O (2015) Pyroclastic density currents: processes and models.
775 In: The Encyclopedia of Volcanoes (pp. 617-629). [https://doi.org/10.1016/B978-0-12-385938-](https://doi.org/10.1016/B978-0-12-385938-9.00035-3)
776 [9.00035-3](https://doi.org/10.1016/B978-0-12-385938-9.00035-3)

777 Esposti Ongaro T, Cerminara M, Charbonnier SJ, Lube G, Valentine G (2020a) A framework for
778 validation and benchmarking of pyroclastic current models. *Bulletin of Volcanology* 82(6):51.
779 <https://doi.org/10.1007/s00445-020-01388-2>

780 Esposti Ongaro T, Komorowski JC, Legendre Y, Neri A (2020b) Modelling pyroclastic density
781 currents from a subplinian eruption at La Soufrière de Guadeloupe (West Indies, France). *Bulletin*
782 *of Volcanology* 82(12):76. <https://doi.org/10.1007/s00445-020-01411-6>

783 Esposti Ongaro T, Orsucci S, Cornolti F (2016) A fast, calibrated model for pyroclastic density
784 currents kinematics and hazard. *Journal of Volcanology and Geothermal Research* 327:257-272.
785 <https://doi.org/10.1016/j.jvolgeores.2016.08.002>

786 Esposti Ongaro T, Widiwijayanti C, Clarke AB, Voight B, Neri A (2011) Multiphase-flow
787 numerical modeling of the 18 May 1980 lateral blast at Mount St. Helens, USA. *Geology*
788 39(6):535-538. <https://doi.org/10.1130/G31865.1>

789 Ferrés D, Delgado-Granados H, Gutiérrez RE, Farraz IA, Hernández EW, Pullinger CR, Escobar
790 CD (2013) Explosive volcanic history and hazard zonation maps of Boquerón Volcano (San
791 Salvador volcanic complex, El Salvador). *Geological Society of America Special Papers*
792 4(498):201-230. [https://doi.org/10.1130/2013.2498\(12\)](https://doi.org/10.1130/2013.2498(12))

793 Gallant E, Richardson J, Connor C, Wetmore P, Connor L (2018) A new approach to probabilistic
794 lava flow hazard assessments, applied to the Idaho National Laboratory, eastern Snake River Plain,
795 Idaho, USA. *Geology* 46(10): 895-898. <https://doi.org/10.1130/G45123.1>

796 Gueugneau V, Charbonnier S, Esposti Ongaro T, de' Michieli Vitturi M, Peruzzetto M, Mangeney
 797 A, Bouchut F, Patra A, Kelfoun K (2021) Synthetic benchmarking of concentrated pyroclastic
 798 current models. *Bulletin of Volcanology* 83:75. <https://doi.org/10.1007/s00445-021-01491-y>
 799 Gertisser R, Charbonnier S, Keller J, Quidelleur X (2012) The geological evolution of Merapi
 800 volcano, Central Java, Indonesia. *Bulletin of Volcanology* 74(5):1213-1233.
 801 <https://doi.org/10.1007/s00445-012-0591-3>
 802 Haccou P, Jagers P, Vatutin VA (2005) Branching processes: variation, growth, and extinction of
 803 populations. Cambridge University Press. <https://doi.org/10.1017/CBO9780511629136>
 804 Harpel CJ, de Silva S, Salas G (2011) The 2 ka eruption of Misti volcano, Southern Peru—the
 805 most recent Plinian eruption of Arequipa's iconic volcano (Vol. 484). Geological Society of
 806 America. <https://doi.org/10.1130/2011.2484>
 807 Harris T (1963) The theory of branching processes. Springer-Verlag Berlin Heidelberg.
 808 Hartmann M (1934) Der grosse Ausbruch des Vulkanes G. Merapi (Mittel Java) im Jahre 1872.
 809 *Vulkanologische und Seismologische Mededeelingen* 13.
 810 Hayashi J, Self S (1992) A comparison of pyroclastic flow and debris avalanche mobility. *Journal*
 811 *of Geophysical Research: Solid Earth* 97(B6):9063-9071. <https://doi.org/10.1029/92JB00173>
 812 Hsu K (1975) Catastrophic debris streams (sturzstroms) generated by rockfalls. *Geological Society*
 813 *of America Bulletin* 86(1):129-140. [https://doi.org/10.1130/0016-](https://doi.org/10.1130/0016-7606(1975)86<129:CDSSGB>2.0.CO;2)
 814 [7606\(1975\)86<129:CDSSGB>2.0.CO;2](https://doi.org/10.1130/0016-7606(1975)86<129:CDSSGB>2.0.CO;2)
 815 Huppert HE, Simpson JE (1980) The slumping of gravity currents. *Journal of Fluid Mechanics*
 816 99(4):785-799. <https://doi.org/10.1017/S0022112080000894>

817 Hyman D, Bevilacqua A, Bursik M (2019) Statistical theory of probabilistic hazard maps: a
818 probability distribution for the hazard boundary location. *Natural Hazard and Earth System*
819 *Sciences* 19:1347-1363. <https://doi.org/10.5194/nhess-19-1347-2019>

820 Isaia R, Vitale S, Marturano A, Aiello G, Barra D, Ciarcia S, Iannuzzi E, Tramparulo FD (2019)
821 High-resolution geological investigations to reconstruct the long-term ground movements in the
822 last 15 kyr at Campi Flegrei caldera (southern Italy). *Journal of Volcanology and Geothermal*
823 *Research* 385:143-158. <https://doi.org/10.1016/j.jvolgeores.2019.07.012>

824 Itoh H, Takahama J, Takahashi M, Miyamoto K (2000) Hazard estimation of the possible
825 pyroclastic flow disasters using numerical simulation related to the 1994 activity at Merapi
826 Volcano. *Journal of Volcanology and Geothermal Research* 100(1-4):503-516.
827 [https://doi.org/10.1016/S0377-0273\(00\)00153-0](https://doi.org/10.1016/S0377-0273(00)00153-0)

828 Jaccard P (1901). Distribution de la flore alpine dans le bassin des Dranses et dans quelques régions
829 voisines. *Bull. Soc. Vaudoise Sci. Nat.* 37:241–272.

830 Kelfoun K (2011) Suitability of simple rheological laws for the numerical simulation of dense
831 pyroclastic flows and long- runout volcanic avalanches. *Journal of Geophysical Research: Solid*
832 *Earth* 116(B8). <https://doi.org/10.1029/2010JB007622>

833 Kelfoun K, Gueugneau V, Komorowski JC, Aisyah N, Cholik N, Merciecca C (2017) Simulation
834 of block- and- ash flows and ash- cloud surges of the 2010 eruption of Merapi volcano with a
835 two- layer model. *Journal of Geophysical Research: Solid Earth* 122(6):4277-4292.
836 <https://doi.org/10.1002/2017JB013981>

837 Kelfoun K, Samaniego P, Palacios P, Barba D (2009) Testing the suitability of frictional behaviour
838 for pyroclastic flow simulation by comparison with a well-constrained eruption at Tungurahua

839 volcano (Ecuador). *Bulletin of Volcanology* 71(9):1057-1075. [https://doi.org/10.1007/s00445-](https://doi.org/10.1007/s00445-009-0286-6)
840 009-0286-6

841 Kelfoun K, Santoso AB, Latchimy T, Bontemps M, Nurdien I, Beauducel F, Fahmi A, Putra R,
842 Dahamna N, Laurin A, Rizal MH, Sukmana JT, Gueugneau V (2021) Growth and collapse of the
843 2018–2019 lava dome of Merapi volcano. *Bulletin of Volcanology* 83(2):1-13.
844 <https://doi.org/10.1007/s00445-020-01428-x>

845 Kennedy MC, O'Hagan A (2001) Bayesian calibration of computer models. *Journal of the Royal*
846 *Statistical Society: Series B (Statistical Methodology)* 63(3):425-464.
847 <https://doi.org/10.1111/1467-9868.00294>

848 Komorowski JC, Jenkins S, Baxter PJ, Picquout A, Lavigne F, Charbonnier S, Gertisser R, Preece
849 K, Cholik N, Budi-Santoso A, Surono (2013) Paroxysmal dome explosion during the Merapi 2010
850 eruption: processes and facies relationships of associated high-energy pyroclastic density currents.
851 *Journal of Volcanology and Geothermal Research* 261:260-294.
852 <https://doi.org/10.1016/j.jvolgeores.2013.01.007>

853 Lavigne F, Morin J, Surono M (2015) *Atlas of Merapi Volcano*. Laboratoire de Géographie
854 Physique, Meudon, France.

855 Lavigne F, Thouret JC, Voight B, Suwa H, Sumaryono A (2000) Lahars at Merapi volcano, Central
856 Java: an overview. *Journal of Volcanology and Geothermal Research* 100(1-4):423-456.
857 [https://doi.org/10.1016/S0377-0273\(00\)00150-5](https://doi.org/10.1016/S0377-0273(00)00150-5)

858 Legros F (2001) Tephra stratigraphy of Misti volcano, Peru. *Journal of South American Earth*
859 *Sciences* 14(1):15-29. [https://doi.org/10.1016/S0895-9811\(00\)00062-6](https://doi.org/10.1016/S0895-9811(00)00062-6)

860 Lirer L, Petrosino P, Alberico I (2001) Hazard assessment at volcanic fields: the Campi Flegrei
861 case history. *Journal of Volcanology and Geothermal Research* 112(1-4):53-73.
862 [https://doi.org/10.1016/S0377-0273\(01\)00234-7](https://doi.org/10.1016/S0377-0273(01)00234-7)

863 Lube G, Breard E, Esposti Ongaro T, Dufek J, Brand B (2020) Multiphase flow behaviour and
864 hazard prediction of pyroclastic density currents. *Nature Reviews Earth & Environment* 1:348-
865 365. <https://doi.org/10.1038/s43017-020-0064-8>

866 Lube G, Cronin SJ, Thouret JC, Surono (2011) Kinematic characteristics of pyroclastic density
867 currents at Merapi and controls on their avulsion from natural and engineered channels. *GSA*
868 *Bulletin* 123(5-6):1127-1140. <https://doi.org/10.1130/B30244.1>

869 Macías JL, Capra L, Arce JL, Espíndola JM, García-Palomo A, Sheridan MF (2008) Hazard map
870 of El Chichón volcano, Chiapas, México: Constraints posed by eruptive history and computer
871 simulations. *Journal of Volcanology and Geothermal Research* 175(4):444-458.
872 <https://doi.org/10.1016/j.jvolgeores.2008.02.023>

873 Malin MC, Sheridan MF (1982) Computer-assisted mapping of pyroclastic surges. *Science*
874 217(4560):637-640. <https://doi.org/10.1126/science.217.4560.637>

875 Mariño J, Rivera M, Cacya L, Thouret JC, Macedo L, Salas G, Siebe C, Tilling R, Sheridan M,
876 Chávez A, Zuñiga S (2008) Mapa de Peligros del Volcán Misti. Instituto Geológico Minero y
877 Metalúrgico (INGEMMET), Direccion de Geologia Ambiental y Riesgo.

878 Martí J, Bartolini S, Becerril L (2016) Enhancing safety in a volcano's shadow. *EOS* 97.
879 <https://doi.org/10.1029/2016EO054161>

880 Mei ETW, Lavigne F, Picquout A, De Bélizal E, Brunstein D, Grancher D, Sartohadi J, Cholik N,
 881 Vidal C (2013) Lessons learned from the 2010 evacuations at Merapi volcano. *Journal of*
 882 *Volcanology and Geothermal Research* 261:348-365.
 883 <https://doi.org/10.1016/j.jvolgeores.2013.03.010>

884 Neri A, Esposti Ongaro T, Voight B, Widiwijayanti C (2015a) Pyroclastic density current hazards
 885 and risk. In: *Volcanic hazards, risks and disasters* (pp. 109-140). Elsevier.
 886 <https://doi.org/10.1016/B978-0-12-396453-3.00005-8>

887 Neri A, Bevilacqua A, Esposti Ongaro T, Isaia R, Aspinall W, Bisson M, Flandoli F, Baxter P,
 888 Bertagnini A, Iannuzzi E, Orsucci S, Pistolesi M, Rosi M, Vitale S (2015b) Quantifying volcanic
 889 hazard at Campi Flegrei caldera (Italy) with uncertainty assessment: 2. Pyroclastic density current
 890 invasion maps. *Journal of Geophysical Research: Solid Earth* 120(4):2330-2349.
 891 <https://doi.org/10.1002/2014JB011776>

892 Neri A, Esposti Ongaro T, de' Michieli Vitturi M, Cerminara M (2022) Multiphase Flow Modeling
 893 of Explosive Volcanic Eruptions. In: *Transport Phenomena in Multiphase Systems* (pp. 243-281).
 894 Springer, Cham. https://doi.org/10.1007/978-3-030-68578-2_10

895 Newhall CG, Bronto S, Alloway B, Banks NG, Bahar I, Del Marmol MA, Hadisantono RD,
 896 Holcomb RT, McGeehin J, Miksic JN, Rubin M, Sayudi SD, Sukhyar R, Andreastuti S, Tilling
 897 RI, Torley R, Trimble D, Wirakusumah AD (2000) 10,000 Years of explosive eruptions of Merapi
 898 Volcano, Central Java: archaeological and modern implications. *Journal of Volcanology and*
 899 *Geothermal Research* 100(1-4):9-50. [https://doi.org/10.1016/S0377-0273\(00\)00132-3](https://doi.org/10.1016/S0377-0273(00)00132-3)

900 Ogburn S, Berger J, Calder E, Lopes D, Patra A, Pitman E, Rutarindwa R, Spiller E, Wolpert R
 901 (2016) Pooling strength amongst limited datasets using hierarchical Bayesian analysis, with

902 application to pyroclastic density current mobility metrics. *Statistics in Volcanology* 2:1-26.
 903 <https://doi.org/10.5038/2163-338X.2.1>

904 Ogburn S, Calder E (2017) The relative effectiveness of empirical and physical models for
 905 simulating the dense undercurrent of pyroclastic flows under different emplacement conditions.
 906 *Frontiers in Earth Science* 5:83. <https://doi.org/10.3389/feart.2017.00083>

907 Orsi G, Di Vito M, Isaia R (2004) Volcanic hazard assessment at the restless Campi Flegrei
 908 caldera. *Bulletin of Volcanology* 66:514-530. <https://doi.org/10.1007/s00445-003-0336-4>

909 Orsi G, Di Vito M, Selva J, Marzocchi W (2009) Long-term forecast of eruption style and size at
 910 Campi Flegrei caldera (Italy). *Earth and Planetary Science Letters* 287(1-2):265-276.
 911 <https://doi.org/10.1016/j.epsl.2009.08.013>

912 Patra A, Bauer A, Nichita C, Pitman E, Sheridan M, Bursik M, Rupp B, Webber A, Stinton A,
 913 Namikawa L, Renschler CS (2005) Parallel adaptive numerical simulation of dry avalanches over
 914 natural terrain. *Journal of Volcanology and Geothermal Research* 139(1-2):1-21.
 915 <https://doi.org/10.1016/j.jvolgeores.2004.06.014>

916 Patra A, Bevilacqua A, Akhavan-Safaei A, Pitman EB, Bursik M, Hyman D (2020) Comparative
 917 analysis of the structures and outcomes of geophysical flow models and modeling assumptions
 918 using uncertainty quantification. *Frontiers in Earth Science* 8:275.
 919 <https://doi.org/10.3389/feart.2020.00275>

920 Poland MP, Anderson KR (2020) Partly cloudy with a chance of lava flows: Forecasting volcanic
 921 eruptions in the twenty- first century. *Journal of Geophysical Research: Solid Earth*
 922 125:e2018JB016974. <https://doi.org/10.1029/2018JB016974>

923 Pudasaini SP, Domnik B (2009) Energy considerations in accelerating rapid shear granular flows.
924 Nonlinear Processes in Geophysics 16:399-407. <https://doi.org/10.5194/npg-16-399-2009>

925 Rivalta E, Corbi F, Passarelli L, Acocella V, Davis T, Di Vito M (2019) Stress inversions to
926 forecast magma pathways and eruptive vent location. Science Advances 5(7).
927 <https://doi.org/10.1126/sciadv.aau9784>

928 Roche O, Phillips J, Kelfoun K (2013) Pyroclastic density currents. In: Modeling Volcanic
929 Processes: The Physics and Mathematics of Volcanism (pp. 203-229).
930 <https://doi.org/10.1017/CBO9781139021562.010>

931 Rossano S, Mastrolorenzo G, De Natale G (2004) Numerical simulation of pyroclastic density
932 currents on Campi Flegrei topography: a tool for statistical hazard estimation. Journal of
933 Volcanology and Geothermal Research 132(1):1-14. [https://doi.org/10.1016/S0377-](https://doi.org/10.1016/S0377-0273(03)00384-6)
934 [0273\(03\)00384-6](https://doi.org/10.1016/S0377-0273(03)00384-6)

935 Rutarindwa R, Spiller E, Bevilacqua A, Bursik M, Patra A (2019) Dynamic probabilistic hazard
936 mapping in the Long Valley Volcanic Region CA: integrating vent opening maps and statistical
937 surrogates of physical models of pyroclastic density currents. Journal of Geophysical Research:
938 Solid Earth 124(9):9600-9621. <https://doi.org/10.1029/2019JB017352>

939 Sandri L, Thouret JC, Constantinescu R, Biass S, Tonini R (2014) Long-term multi-hazard
940 assessment for El Misti volcano (Peru). Bulletin of Volcanology 76(2):1-26.
941 <https://doi.org/10.1007/s00445-013-0771-9>

942 Sandri L, Tierz P, Costa A, Marzocchi W (2018) Probabilistic hazard from pyroclastic density
943 currents in the Neapolitan area (Southern Italy). Journal of Geophysical Research: Solid Earth
944 123(5):3474-3500. <https://doi.org/10.1002/2017JB014890>

945 Sayudi DS, Nurnaning A, Juliani D, Muzani M (2010) Peta Kawasan Rawan Bencana Gunungapi
 946 Merapi, Jawa Tengah Dan Daerah Istimewa Yogyakarta 2010. Center for Volcanology and
 947 Geological Hazard Mitigation.

948 Scollo S, Tarantola S, Bonadonna C, Coltelli M, Saltelli A (2008) Sensitivity analysis and
 949 uncertainty estimation for tephra dispersal models. *Journal of Geophysical Research: Solid Earth*
 950 113(B6). <https://doi.org/10.1029/2006JB004864>

951 Selva J, Orsi G, Di Vito M, Marzocchi W, Sandri L (2012) Probability hazard map for future vent
 952 opening at the Campi Flegrei caldera, Italy. *Bulletin of Volcanology* 74(2):497-510.
 953 <https://doi.org/10.1007/s00445-011-0528-2>

954 Sheridan M, Hubbard B, Carrasco-Núñez G, Siebe C (2004) Pyroclastic flow hazard at Volcán
 955 Citlaltépetl. *Natural Hazards* 33:209-221. <https://doi.org/10.1023/B:NHAZ.0000037028.89829.d1>

956 Sheridan M, Macías JL (1995) Estimation of risk probability for gravity-driven pyroclastic flows
 957 at Volcan Colima, Mexico. *Journal of Volcanology and Geothermal Research* 66(1-4):251-256.
 958 [https://doi.org/10.1016/0377-0273\(94\)00058-O](https://doi.org/10.1016/0377-0273(94)00058-O)

959 Sheridan M, Malin M (1983) Application of computer-assisted mapping to volcanic hazard
 960 evaluation of surge eruptions: Vulcano, Lipari, and Vesuvius. *Journal of Volcanology and*
 961 *Geothermal Research* 17(1-4):187-202. [https://doi.org/10.1016/0377-0273\(83\)90067-7](https://doi.org/10.1016/0377-0273(83)90067-7)

962 Smith V, Isaia R, Pearce N (2011) Tephrostratigraphy and glass compositions of post-15 kyr
 963 Campi Flegrei eruptions: implications for eruption history and chronostratigraphic markers.
 964 *Quaternary Science Reviews* 30(25-26):3638-3660.
 965 <https://doi.org/10.1016/j.quascirev.2011.07.012>

966 Solikhin A (2015) Geology, tectonics and post-2001 eruptive activity interpreted from high-spatial
967 resolution satellite imagery: the case study of Merapi and Seremu volcanoes, Indonesia. PhD.
968 Thesis, Earth Sciences. Université Blaise Pascal - Clermont-Ferrand II.

969 Spiller E, Bayarri M, Berger J, Calder E, Patra A, Pitman E, Wolpert R (2014) Automating
970 emulator construction for geophysical hazard maps. SIAM/ASA Journal on Uncertainty
971 Quantification 2(1):126-152. <https://doi.org/10.1137/120899285>

972 Surono, Jousset P, Pallister J, Boichu M, Buongiorno MF, Budisantoso A, Costa F, Andreastuti S,
973 Prata F, Schneider D, Clarisse L, Humaida H, Sumarti S, Bignami C, Griswold J, Carn S,
974 Oppenheimer C, Lavigne F (2012) The 2010 explosive eruption of Java's Merapi volcano—a '100-
975 year' event. Journal of Volcanology and Geothermal Research 241-242:121-135.
976 <https://doi.org/10.1016/j.jvolgeores.2012.06.018>

977 Tadini A, Bevilacqua A, Neri A, Cioni R, Biagioli G, de' Michieli Vitturi M, Esposti Ongaro T
978 (2021) Reproducing pyroclastic density current deposits of the 79 CE eruption of the Somma–
979 Vesuvius volcano using the box-model approach. Solid Earth 12(1):119-139.
980 <https://doi.org/10.5194/se-12-119-2021>

981 Takarada, S. (2017). The volcanic hazards assessment support system for the online hazard
982 assessment and risk mitigation of quaternary volcanoes in the world. Frontiers in Earth Science
983 5:102. <https://doi.org/10.3389/feart.2017.00102>

984 Thouret JC, Lavigne F, Kelfoun K, Bronto S (2000) Toward a revised hazard assessment at Merapi
985 volcano, Central Java. Journal of Volcanology and Geothermal Research 100(1-4):479-502.
986 [https://doi.org/10.1016/S0377-0273\(00\)00152-9](https://doi.org/10.1016/S0377-0273(00)00152-9)

987 Thouret JC, Finizola A, Fornari M, Legeley-Padovani A, Suni J, Frechen M (2001) Geology of El
988 Misti volcano near the city of Arequipa, Peru. *Geological Society of America Bulletin*
989 113(12):1593-1610. [https://doi.org/10.1130/0016-7606\(2001\)113<1593:GOEMVN>2.0.CO;2](https://doi.org/10.1130/0016-7606(2001)113<1593:GOEMVN>2.0.CO;2)

990 Tierz P, Sandri L, Costa A, Sulpizio R, Zaccarelli L, Di Vito M, Marzocchi W (2016a) Uncertainty
991 assessment of pyroclastic density currents at Mount Vesuvius (Italy) simulated through the energy
992 cone model. *Natural Hazard Uncertainty Assessment: Modeling and Decision Support* 223:125-
993 145.

994 Tierz P, Sandri L, Costa A, Zaccarelli L, Di Vito M, Sulpizio R, Marzocchi W (2016b) Suitability
995 of energy cone for probabilistic volcanic hazard assessment: validation tests at Somma-Vesuvius
996 and Campi Flegrei (Italy). *Bulletin of Volcanology* 78(11):1-15. [https://doi.org/10.1007/s00445-](https://doi.org/10.1007/s00445-016-1073-9)
997 016-1073-9

998 Tierz P, Stefanescu ER, Sandri L, Sulpizio R, Valentine GA, Marzocchi W, Patra AK (2018).
999 Towards quantitative volcanic risk of pyroclastic density currents: Probabilistic hazard curves and
1000 maps around Somma-Vesuvius (Italy). *Journal of Geophysical Research: Solid Earth* 123:6299–
1001 6317. <https://doi.org/10.1029/2017JB015383>

1002 Todesco M, Neri A, Esposti Ongaro T, Papale P, Rosi M (2006) Pyroclastic flow dynamics and
1003 hazard in a caldera setting: Application to Phlegrean Fields (Italy). *Geochemistry, Geophysics,*
1004 *Geosystems* 7(11). <https://doi.org/10.1029/2006GC001314>

1005 Tonini R, Sandri L, Thompson MA (2015) PyBetVH: A Python tool for probabilistic volcanic
1006 hazard assessment and for generation of Bayesian hazard curves and maps. *Computers &*
1007 *Geosciences* 79:38-46. <https://doi.org/10.1016/j.cageo.2015.02.017>

1008 Valentine G (2019) Preface to the topical collection—pyroclastic current models: benchmarking
 1009 and validation. *Bulletin of Volcanology* 81:69. <https://doi.org/10.1007/s00445-019-1328-3>

1010 Voight B, Constantine E, Siswowidjoyo S, Torley R (2000) Historical eruptions of Merapi
 1011 volcano, central Java, Indonesia, 1768–1998. *Journal of Volcanology and Geothermal Research*
 1012 100(1-4):69-138. [https://doi.org/10.1016/S0377-0273\(00\)00134-7](https://doi.org/10.1016/S0377-0273(00)00134-7)

1013 Voight B, Davis MJ (2000) Emplacement temperatures of the November 22, 1994 nuée ardente
 1014 deposits, Merapi Volcano, Java. *Journal of Volcanology and Geothermal Research* 100(1-4):371-
 1015 377. [https://doi.org/10.1016/S0377-0273\(00\)00146-3](https://doi.org/10.1016/S0377-0273(00)00146-3)

1016 Wadge G, Isaacs M (1988) Mapping the volcanic hazards from Soufriere Hills Volcano,
 1017 Montserrat, West Indies using an image processor. *Journal of the Geological Society* 145(4):541-
 1018 551. <https://doi.org/10.1144/gsjgs.145.4.0541>

1019 White JT, Connor CB, Connor L, Hasenaka T (2017) Efficient inversion and uncertainty
 1020 quantification of a tephra fallout model. *Journal of Geophysical Research: Solid Earth* 122(1):281-
 1021 294. <https://doi.org/10.1002/2016JB013682>

1022 Worni R, Huggel C, Stoffel M, Pulgarín B (2012) Challenges of modeling current very large lahars
 1023 at Nevado del Huila Volcano, Colombia. *Bulletin of Volcanology* 74(2):309-324.
 1024 <https://doi.org/10.1007/s00445-011-0522-8>

1025 Yang Q, Pitman E, Spiller E, Bursik M, Bevilacqua A (2020) Novel statistical emulator
 1026 construction for volcanic ash transport model Ash3d with physically motivated measures.
 1027 *Proceedings of the Royal Society A* 476(2242):20200161. <https://doi.org/10.1098/rspa.2020.0161>

Figure Captions

Figure 1. Illustrative example of the tree-like structure used in the branching energy cone model. More details can be found in Aravena et al. (2020). Left-hand side: surface plots of the energy cones and the topography. Central column: contour plots of the energy cones and the topography. Right-hand side: functions of horizontal distance (i.e. run-out distance as a function of the polar angle) of the different generations of energy cones. The number of generations increases from top to bottom.

Figure 2. Illustrations of the different metrics used to calculate the similarity index between a reference scenario, defined by the reference inundation polygon A, and a given calibration simulation characterized by the inundation polygon B (see Section 3.1). In panel c, the intersection of polygons A and B is indicated in green, while the union of these polygons is represented by the sum of green and red areas.

Figure 3. (a) Elevation map of El Misti volcano (Peru) including the PDC inundation area associated with the 2070 cal yr BP eruption (Charbonnier et al. 2020), used to calibrate the branching energy cone model. The red point represents the collapse position used in the calibration simulations. (b-d) Pseudo-color plots of the different coincidence parameters (RMSD, HD and JI) computed from the calibration simulations. In these panels, yellow pixels are associated with high similarity indexes between the calibration simulations and the reference inundation polygon, and blue pixels indicate low degrees of similarity between the computed invasion zones in the calibration simulations and the reference inundation polygon. RMSD and HD are expressed in meters in the color scales, while JI is a non-dimensional coincidence parameter. (e-g) Sampling probability distributions of input parameters ($H_{0,0}$ and $\tan(\varphi)$) used in different sets of simulations for El Misti volcano (see Fig. 4), which derive from the calibrations simulations displayed in panels b-d. Values in the color scales represent the sampling probability per cell, where each cell corresponds to one hundredth of the variation range of each calibrated input of the model (i.e. $H_{0,0}$ and $\tan(\varphi)$).

Figure 4. Maps of PDC inundation probability at El Misti volcano imported in a GIS environment. Results are expressed in percent. Intense red tones indicate high PDC inundation probability. The input parameters used in these

simulations derive from the calibrations displayed in Figure 3. The reference PDC deposit used for the numerical calibration of input parameters is displayed in green (2070 cal yr BP eruption; Charbonnier et al. 2020).

Figure 5. (a-b) Pseudo-color plots of runout distance and inundation area derived from the set of calibration simulations performed for Merapi volcano. Runout distance is expressed in km in the color scale. (c-d) PDF and CDF of the predefined probability distributions of runout distance adopted for the calibration of input parameters used in Merapi simulations. These distributions derive from fitting the data of 55 PDCs (Solikhin 2015), which are displayed as a histogram (c) and an empirical cumulative curve (d), using gamma and lognormal probability distributions. In panel d, $F(x)$ denotes the cumulative distribution of runout distance. (e-f) Sampling probability distribution of input parameters ($H_{0,0}$ and $\tan(\varphi)$) used in two sets of simulations performed for Merapi volcano (see Fig. 6). Values in the color scales represent the sampling probability per cell, where each cell corresponds to one hundredth of the variation range of each calibrated input of the model (i.e. $H_{0,0}$ and $\tan(\varphi)$).

Figure 6. Probability maps of PDC inundation at Merapi volcano constructed using the branching energy cone model. Collapse positions were sampled uniformly within a 300 m-radius circle in the volcanic summit while collapse parameters (i.e. $H_{0,0}$ and $\tan(\varphi)$) were sampled considering the distribution of runout distance observed in the geological record (Solikhin 2015). This data was fitted using gamma (a) and lognormal (b) probability distributions (Fig. 5c-f). Results of PDC inundation probability, indicated in the isolines, are expressed in percent.

Figure 7. Empirical cumulative curves of runout distance in documented PDCs at Merapi and in the simulation sets presented in Figure 6. The predefined probability functions of runout distance, derived from fitting the data of documented PDCs (Solikhin 2015) using both gamma and lognormal probability functions, are included. The differences between these curves are mainly related to the absence of runout distances lower than 2.5 km in the modeling results. $F(x)$ denotes the cumulative distribution of runout distance.

Figure 8. (a) Map of Campi Flegrei showing the points used as the collapse position in the calibration simulations. (b-c) Pseudo-color plots of inundation area derived from the set of calibration simulations performed for Campi Flegrei. Inundation area is expressed in km^2 in the color scale. (d-e) CDFs of the inundation area in documented PDCs at the western and eastern domains of Campi Flegrei and the expected probability distributions of this parameter, computed following Neri et al. (2015b) and Bevilacqua et al. (2017) in order to consider the effect of likely

underestimations of the area of PDC deposits and the presence of “lost” deposits in the dataset. In panels d and f, $F(x)$ denotes the cumulative distribution of inundation area.

Figure 9. Sampling probability distributions of input parameters (collapsing volume and initial concentration of solid particles) in two sets of simulations performed for Campi Flegrei (see Fig. 10). Values in the color scales represent the sampling probability per cell, where each cell corresponds to one hundredth of the variation range of each calibrated input of the model (i.e. $\log(V_0)$ and ϕ_0).

Figure 10. Probability maps of PDC inundation at Campi Flegrei constructed using the traditional box model. Collapse positions were sampled from published vent opening probability maps (Neri et al. 2015b; Bevilacqua et al. 2017), while the other model inputs were sampled considering calibrations based on the expected distribution of inundation area. Results of PDC inundation probability, indicated in the isolines, are expressed in percent.

Figure 11. CDFs of the inundation area in documented PDCs at the western and eastern domains of Campi Flegrei, the expected probability distributions of this parameter (i.e. prescribed in our numerical simulations), and the resulting distributions of inundation area in the simulations presented in Figure 10. $F(x)$ denotes the cumulative distribution of inundation area.

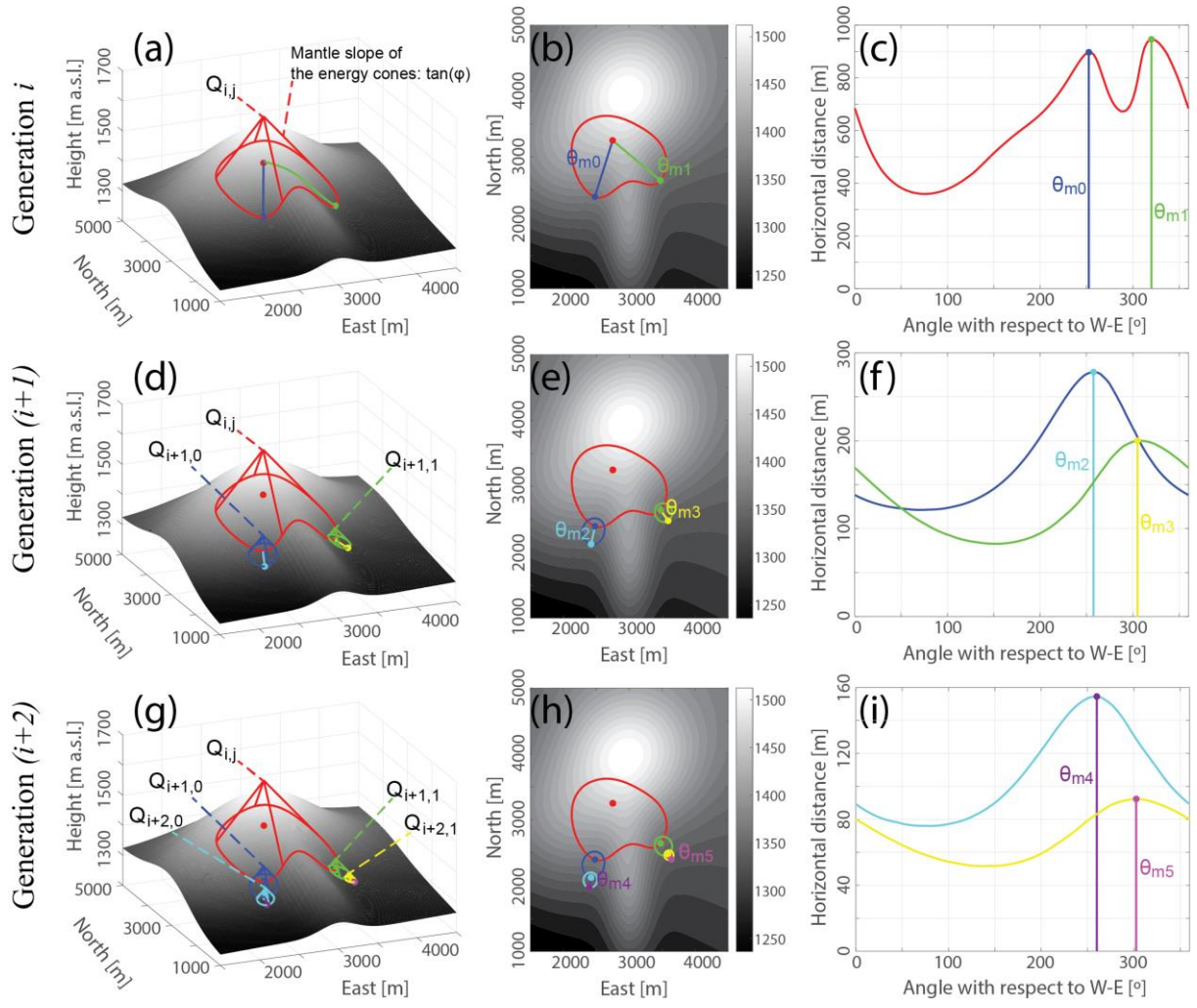
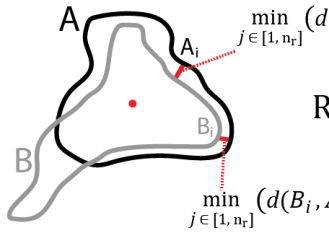


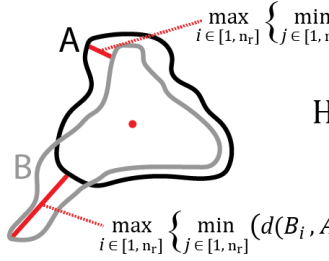
Figure 1.

(a) Root mean square distance (RMSD)



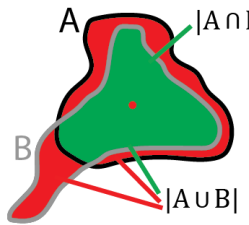
$$\text{RMSD} = \frac{\left(\left(\sum_{i=1}^{n_r} \min_{j \in [1, n_r]} (d(A_i, B_j))^2 \right) + \left(\sum_{i=1}^{n_r} \min_{j \in [1, n_r]} (d(B_i, A_j))^2 \right) \right)^{0.5}}{2n_r}$$

(b) Hausdorff distance (HD)



$$\text{HD} = \max \left\{ \max_{i \in [1, n_r]} \left\{ \min_{j \in [1, n_r]} (d(A_i, B_j)) \right\}, \max_{i \in [1, n_r]} \left\{ \min_{j \in [1, n_r]} (d(B_i, A_j)) \right\} \right\}$$

(c) Jaccard Index (JI)



$$\text{JI} = \frac{|A \cap B|}{|A \cup B|}$$

Figure 2.

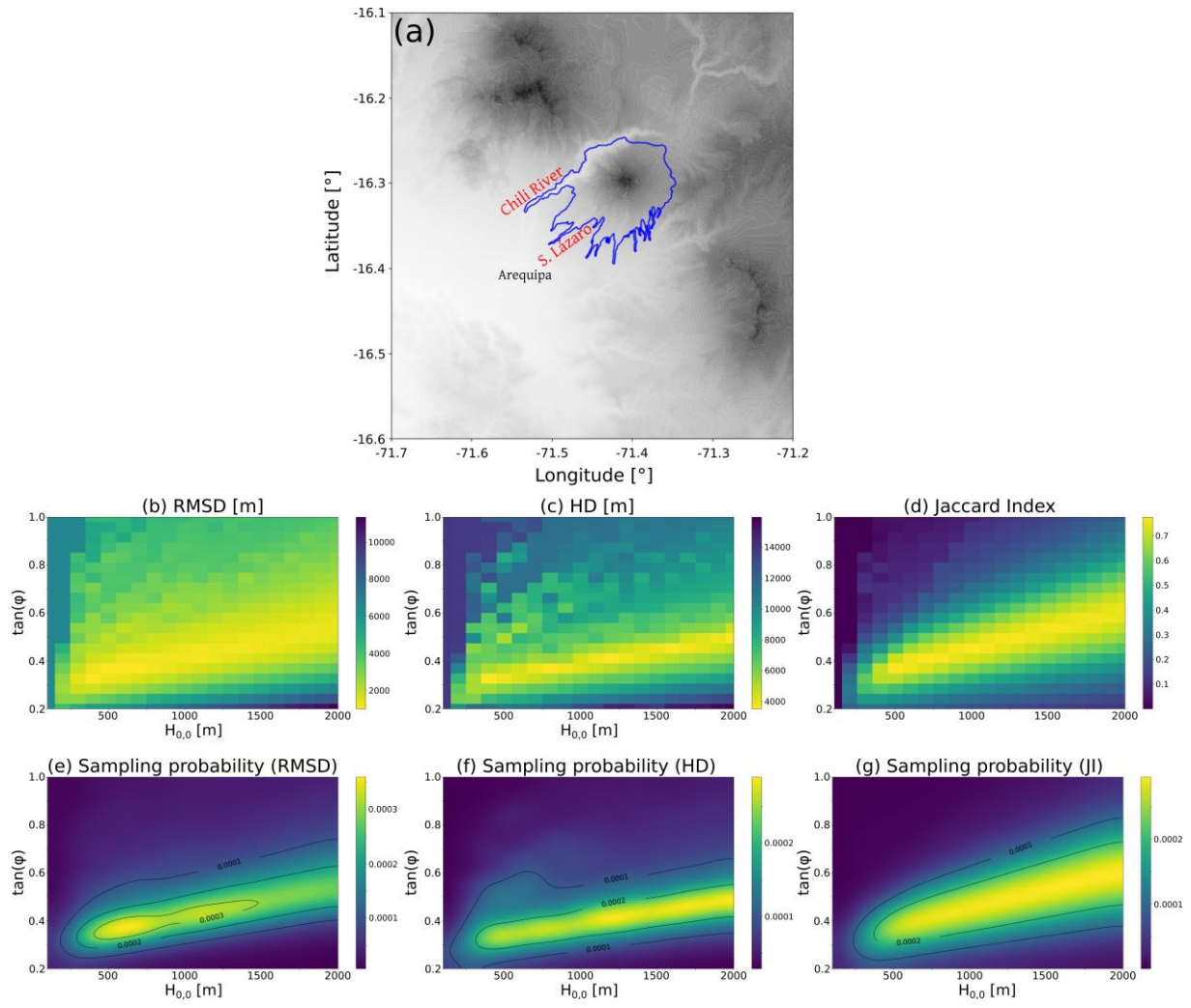


Figure 3.

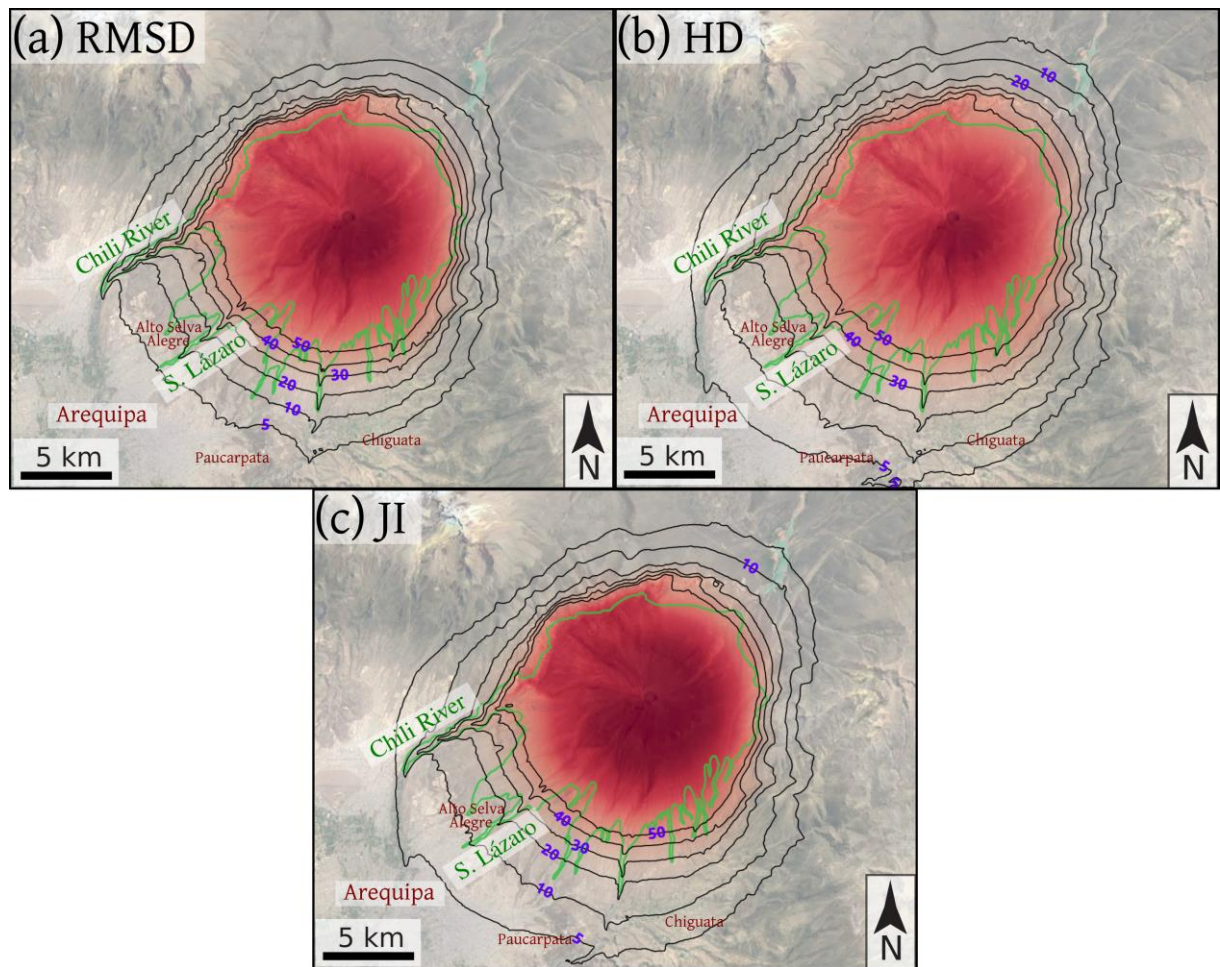


Figure 4.

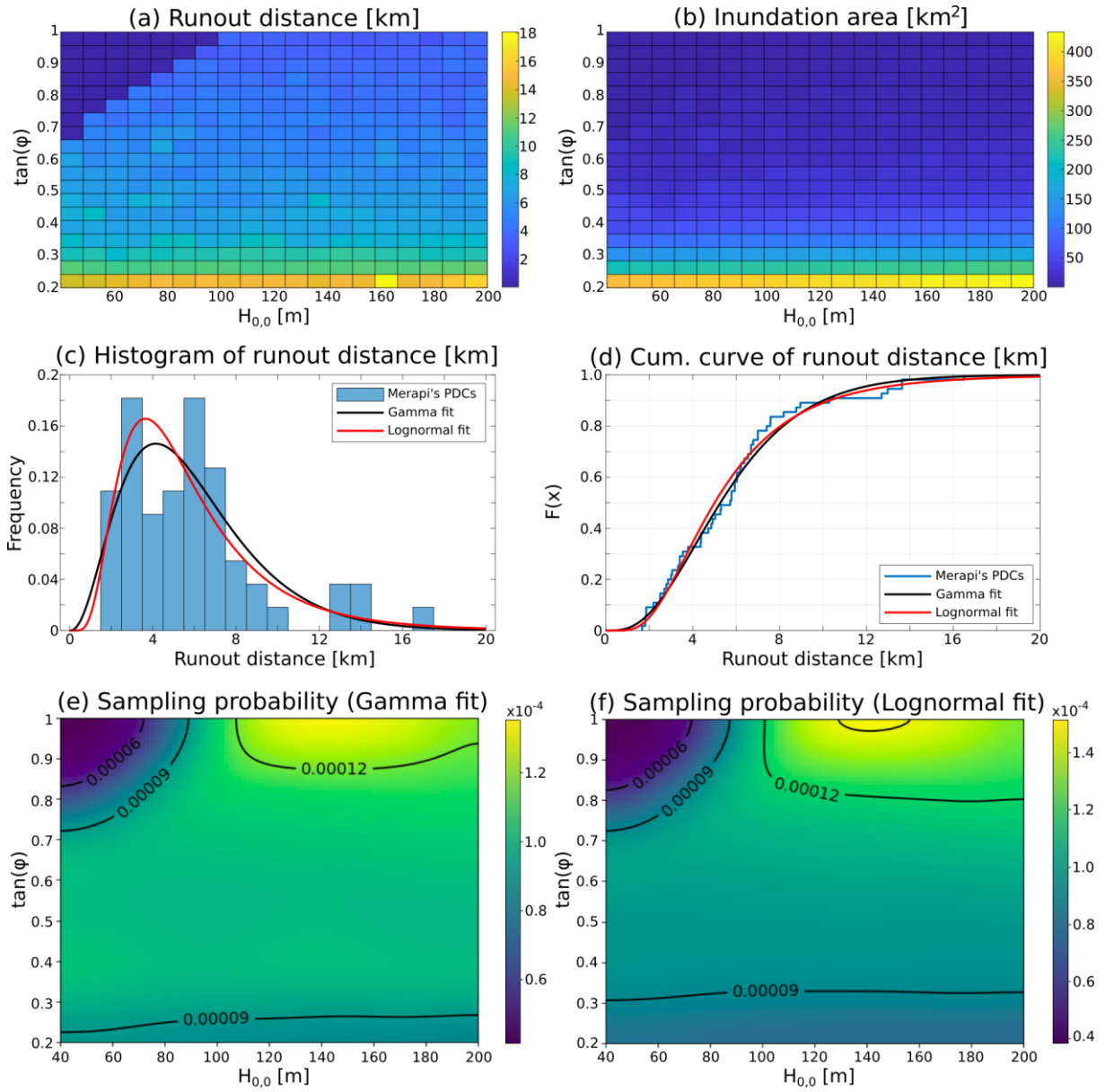


Figure 5.

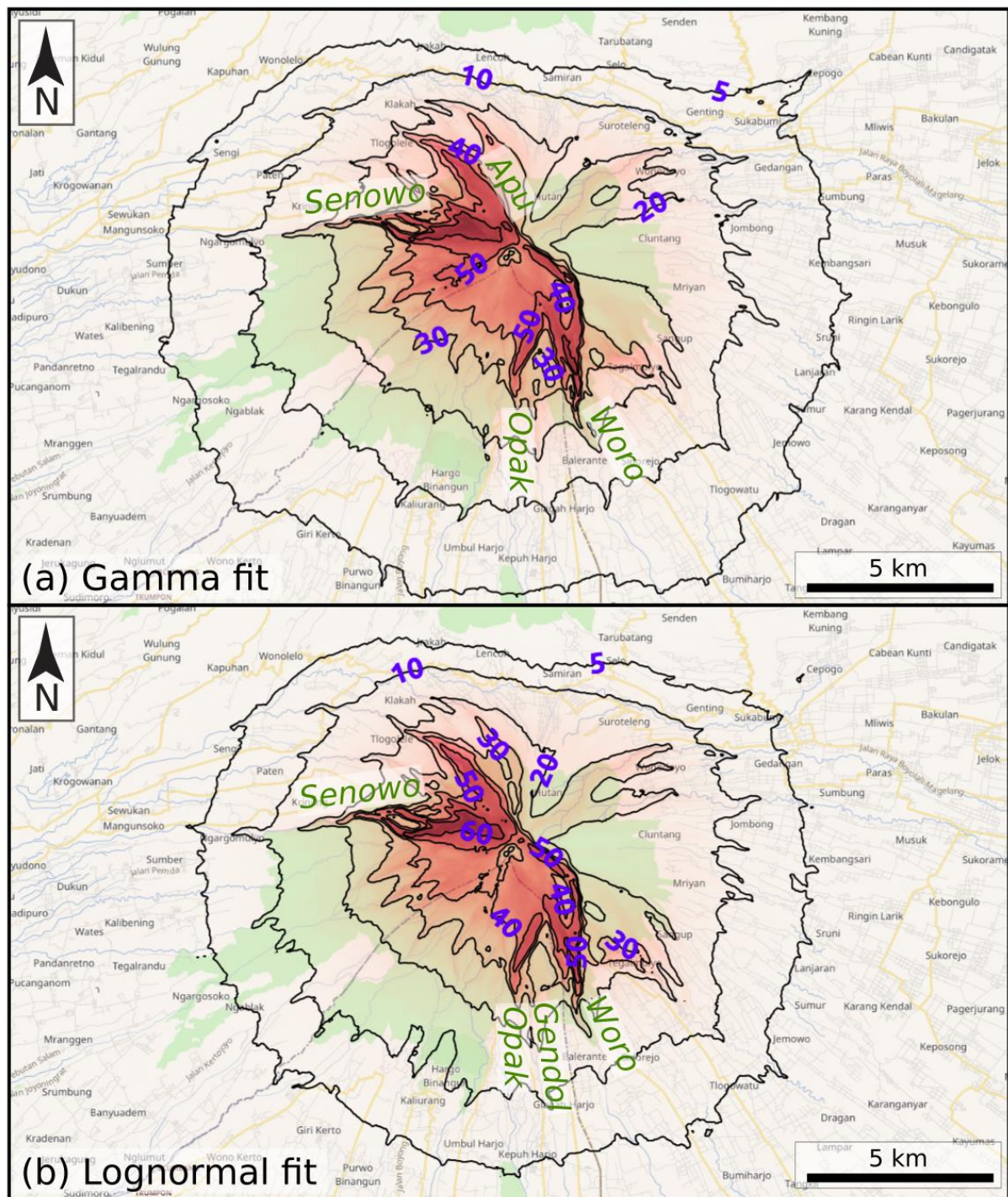


Figure 6.

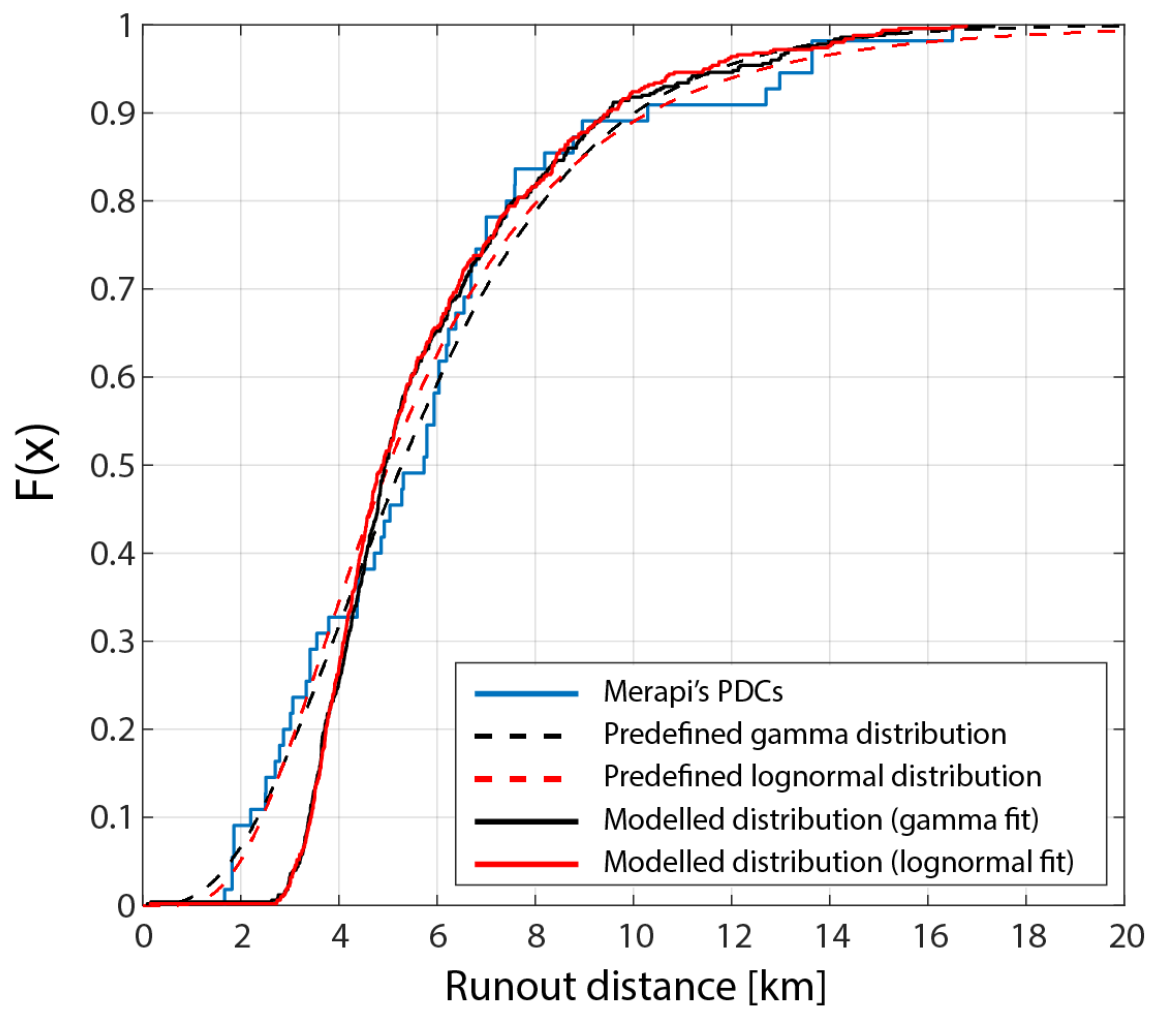


Figure 7.

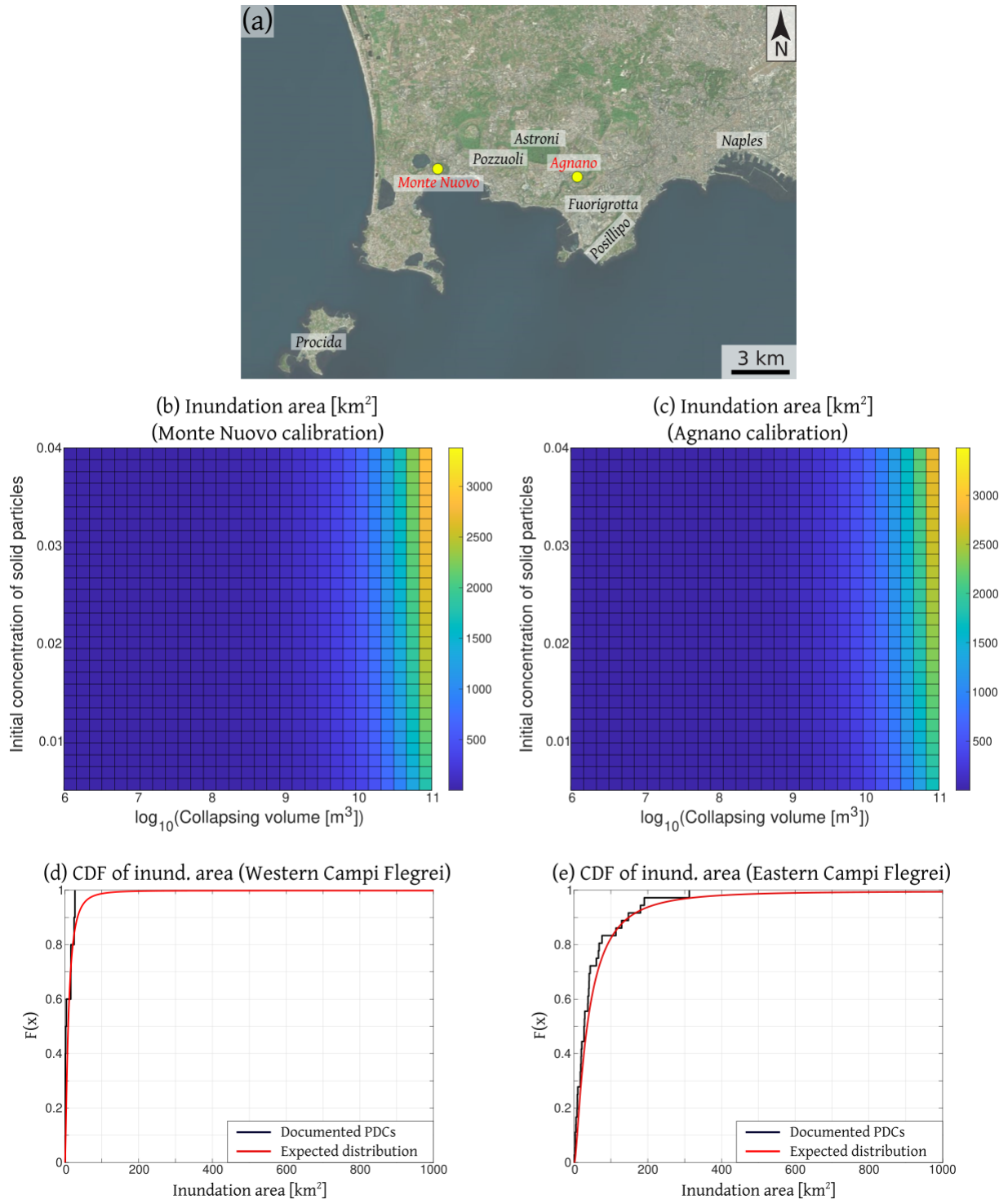


Figure 8.

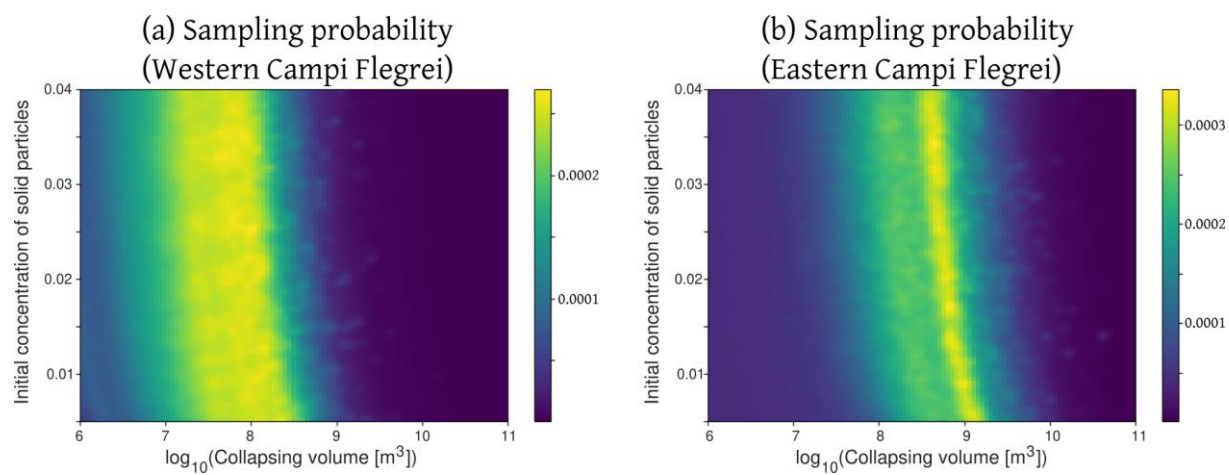


Figure 9.

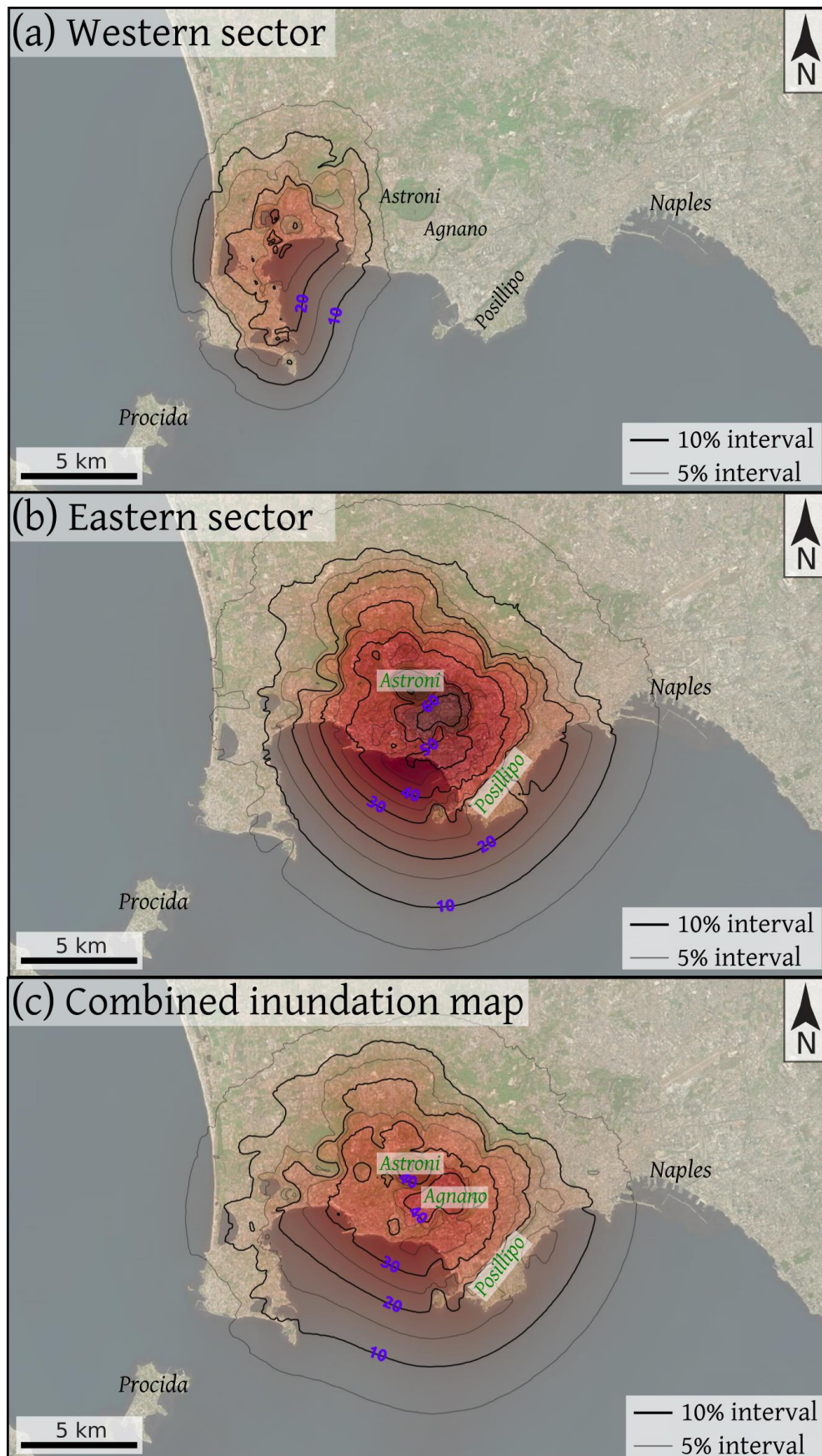


Figure 10.

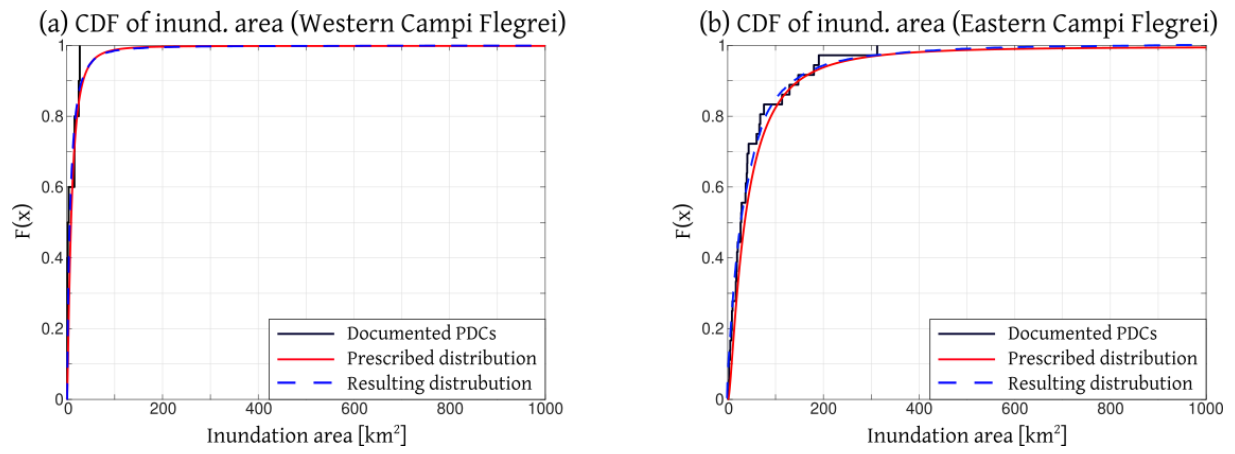


Figure 11.